## Along-Strike Variations of Alaska Subduction Zone Structure and Hydration 1 **Determined From Amphibious Seismic Data** 2 3 Zongshan Li<sup>1</sup>, Douglas A. Wiens<sup>1</sup>, Weisen Shen<sup>2</sup>, Donna J. Shillington<sup>3</sup> 4 <sup>1</sup>Department of Earth, Environmental, and Planetary Sciences, Washington University, St. Louis, 5 MO 63130, USA. 6 <sup>2</sup>Department of Geosciences, Stony Brook University, Stony Brook, NY 11794, USA. 7 <sup>3</sup>School of Earth and Sustainability, Northern Arizona University, Flagstaff, AZ 86011, USA. 8 9 Corresponding author: Zongshan Li (zongshan.li@wustl.edu) 10 11 12

# **Key Points:**

13

14

15

16

17

- Crustal thickness of the inner forearc (35-42 km) generally exceeds that of the volcanic arc, but becomes variable in the Shumagin segment.
- The Shumagin segment has more incoming plate mantle hydration than the Semidi segment, aligning with abundant plate bending normal faults.
- Hydration extends to depths of 18 km below the Moho, indicating more water subducts than most previous estimates.

#### Abstract

We develop a 3-D isotropic shear velocity model for the Alaska subduction zone using data from seafloor and land-based seismographs to investigate along-strike variations in structure. By applying ambient noise and teleseismic Helmholtz tomography, we derive Rayleigh wave group and phase velocity dispersion maps, then invert them for shear velocity structure using a Bayesian Monte Carlo algorithm. For land-based stations, we perform a joint inversion of receiver functions and dispersion curves. The forearc crust is relatively thick (35-42 km) and has reduced lower crustal velocities beneath the Kodiak and Semidi segments, which may promote higher seismic coupling. Bristol Bay Basin crust is relatively thin and has a high-velocity lower layer, suggesting a dense mafic lower crust emplaced by the rifting processes. The incoming plate shows low uppermost mantle velocities, indicating serpentinization. This hydration is more pronounced in the Shumagin segment, with greater velocity reduction extending to  $18 \pm 3$  km depth, compared to the Semidi segment, showing smaller reductions extending to  $14 \pm 3$  km depth. Our estimates of percent serpentinization from V<sub>S</sub> reduction and V<sub>P</sub>/V<sub>S</sub> are larger than those determined using V<sub>P</sub> reduction in prior studies, likely due to water in cracks affecting V<sub>S</sub> more than V<sub>P</sub>. Revised estimates of serpentinization show that more water subducts than previous studies, and that twice as much mantle water is subducted in the Shumagin segment compared to the Semidi segment. Together with estimates from other subduction zones, the results indicate a wide variation in subducted mantle water between different subduction segments.

## Plain Language Summary

This study uses seismic data from the 2018-2019 Alaska Amphibious Community Seismic Experiment and other land stations to image the 3-D seismic velocity structure of the Alaska subduction zone. The analysis combines constraints from both Rayleigh waves and converted body waves. The results provide insight into the distinct lateral variations observed for many properties of the subduction zone. Thick, low-velocity forearc crust is found beneath the Kodiak and Semidi segments, which may be related to the higher seismic coupling in these regions. The Bristol Bay Basin has a thin crust with a high velocity lower layer, suggesting a dense mafic lower crust emplaced by the extensional processes that formed the basin. Low velocities in the incoming plate near the trench in the Shumagin segment indicate pronounced mantle hydration, extending to about 18 km below the Moho. Together with estimates from other subduction zones, the results indicate a wide variation in subducted mantle water between different subduction segments.

#### 1 Introduction

Subduction zones are the locus of many of the most important geological processes, including earthquakes, volcanism, sediment accretion, and the formation of new crust. It is particularly useful to study the along-strike variability of these parameters within a single large subduction segment. The Alaska subduction zone is one of the most tectonically active plate boundaries worldwide, with numerous large earthquakes and active volcanoes. In the Alaska Peninsula region, the subducting plate has an intermediate age (~50-55 Ma) and a relatively uniform convergence rate (~63 mm/yr) (DeMets et al., 2010), but the seismicity, geodetic

locking, and earthquake rupture zones show distinct along-strike variations (e.g., Davies et al., 1981; Shillington et al., 2015; Xiao et al., 2021) (Figure 1). These along-strike variations make it an ideal place to study many subduction zone processes, including earthquake and geodetic properties, forearc and backarc tectonics, and the pathways of water through the subduction system. Many aspects of the along-strike variations in these processes can be revealed by detailed imaging of variations in subduction zone structure.

Subduction zones are also the key to understanding the long-term water cycle on Earth, since subducting oceanic plate serves as the only mechanism to carry water into the deep interior of the Earth. The water flux from hydrated oceanic plates is essential for arc volcanism and may control along-arc changes in magma chemistry (Sadofsky et al., 2008; Manea et al., 2014). Furthermore, water greatly lowers the viscosity of the surrounding mantle, which is important for the dynamics of subduction (e.g., Hebert et al., 2009). Hydration of downgoing slabs is likely to be ubiquitous in the worldwide oceanic trench regions, but the degree and extent of mantle hydration is poorly constrained, and remains the main uncertainty in the global water cycle (van Keken et al., 2011). A previous study of the Alaska subduction zone suggested strong along-strike variations in mantle hydration of the incoming plate in the offshore Alaska Peninsula region (Shillington et al, 2015).

Active-source studies have revealed low mantle velocities in the plate-bending regions of many subduction zones that are interpreted as indicating serpentinization of mantle peridotite (Ranero et al., 2003; Van Avendonk et al., 2011; Shillington et al., 2015; Fujie et al., 2018; Arnulf et al., 2022), including offshore of the Shumagin segment (Shillington et al., 2015; Acquisto et al., 2022b; Shillington et al., 2022). However, in most cases active-source studies provide only limited constraints on the depth extent of mantle serpentinization, leaving large uncertainties in the amount of bound water subducted. Passive-source studies, on the other hand, are able to image the deeper structure of the incoming plate and place constraints on the depth of serpentinization. A passive source study in the Mariana subduction zone found that the mantle hydration at the Mariana trench extends to ~24 km below the Moho (Cai et al., 2018), suggesting the total amount of water input into the Mariana trench is at least 4.3 times more than previous estimates (van Keken et al., 2011). Since the Alaska Subduction Zone differs from Mariana in terms of incoming plate age (~50 Ma, as opposed to ~150 Ma for Mariana), and shows extensive along-strike variation in incoming plate fabric and faulting, it represents an excellent target to test the possible widespread occurrence of deeper incoming plate hydration.

The 2018-2019 Alaska Amphibious Community Seismic Experiment (AACSE) deployed an amphibious array of 75 ocean bottom seismographs (OBS) and 30 land seismographs, complemented by a temporary nodal array on Kodiak Island and an active-source seismic experiment offshore the Semidi segment and Kodiak Island (Barcheck et al., 2020). The amphibious array of AACSE, along with several other simultaneously operating land seismic networks, provide a unique opportunity to image subduction zone structure. In this study, we use this dataset to image the along-strike variations in the Alaska subduction zone structure and provide important constraints on the hydration of the downgoing plate, as well as the structure and tectonics of the forearc and backarc regions. In contrast to previous surface wave tomographic studies that carry out large-scale imaging of the entire Alaska region, or analyze only one type of seismic data, our analysis includes both ambient noise tomography and teleseismic earthquake Helmholtz tomography, as well as P-wave receiver functions, to better constrain the Alaska subduction zone with higher resolution.

109 2 Tectonic Setting and Previous Work

From west to east, the plate boundary can be divided into three main segments, named Shumagin, Semidi, and Kodiak segments after the corresponding forearc islands (Figure 1b). The Shumagin segment, also called the Shumagin Gap, is a region with abundant interplate and intermediate-depth earthquakes (Figure 1a), but has not ruptured during a great earthquake ( $M \ge 1$ 8) for at least 150 years (Davies et al., 1981). The Semidi and Kodiak segments, however, have much less seismicity at all depths and have ruptured in several historical great earthquakes (e.g., 1938 M8.2; 1946 M8.6; 1964 M9.2) (Davies et al., 1981) (Figure 1b). In recent years, two megathrust events (July 22, 2020 M7.8 Simeonof earthquake and July 29, 2021 M8.2 Chignik earthquake) occurred in the Semidi segment (Figure 1b). The slip model of the 2021 M8.2 Chignik earthquake suggests that its rupture zone is within the estimated 1938 M8.2 aftershock zone (Chengli Liu et al., 2022; He et al., 2023). The 2020 M7.8 Simeonof earthquake, however, expanded westward and is considered to have ruptured the eastern Shumagin Gap and a little bit of the westernmost Semidi segment (Liu et al., 2020), and was followed by an unusual strike-slip M7.6 event within the Shumagin Gap on October 19, 2020 (Y. Jiang et al., 2022). In addition, geodetic results suggest that the plate motion along the megathrust changes from creeping nearly aseismically in the western portion of the Shumagin segment, to weakly coupled in the eastern portion of the Shumagin segment, to intermediate coupled in the Semidi segment, to strongly locked in the Kodiak segment (S. Li & Freymueller, 2018; Drooff & Freymueller, 2021; Xiao et al., 2021). The characteristics of double seismic zones (DSZs) also show clear variations between each segment (Wei et al., 2021; Aziz Zanjani & Lin, 2022).

The distribution of incoming plate fabric, sediment thickness, and plate bending faults are also highly variable along the strike. The incoming plate fabric has a variable orientation resulting from the spreading along the Kula plate and Kula-Farallon ridge (e.g., Lonsdale, 1988; Bradley et al., 2003). Magnetic anomalies on the incoming Pacific plate show that the paleospreading direction changes from sub-parallel to the trench axis in the Shumagin segment to sub-perpendicular to the trench axis in the Semidi and Kodiak segments (Figure 1a). As for the sediment thickness of the incoming plate, the Shumagin segment has disrupted sediments (~0.5 km) while the Semidi segment has relatively thick and stable sediment (~1 km) (Shillington et al., 2015; J. Li et al., 2018). Furthermore, the Shumagin segment shows abundant outer-rise faults whereas the Semidi and Kodiak segments have few outer-rise faults (Shillington et al., 2015).

A previous active source study compared profiles between Shumagin and Semidi segments, finding much stronger velocity reduction and thus hydration in the Shumagin segment (Shillington et al., 2015; Shillington et al., 2022). They suggest that hydration is controlled by the intensity of plate-bending faults, which is in turn strongly influenced by the plate abyssal hill fabric formed during spreading (e.g., D. H. Christensen & Ruff, 1988; Masson, 1991; Ranero et al., 2003). Small faults from the plate spreading fabric are parallel to magnetic anomalies, being oriented roughly trench-parallel in the Shumagin segment but at high angles to the trench axis in the Semidi segment (Figure 1; Figure 8a). However, other studies suggest that factors like the trench-ridge angle (Fujie et al., 2018), or slab curvature (Naliboff et al., 2013) may be more important in controlling the along-strike variation.

The overriding plate in the Alaska Peninsula is built from a series of accreted terranes, including the Peninsula Terrance, the Chugach Terrane, and the younger Prince William Terrane (Bruns et al., 1985; Horowitz et al., 1989) (Figure 1c). Active-source projects EDGE (Moore et al., 1991) and ALEUT (Shillington et al., 2015; Bécel et al., 2017) have revealed variations in Pwave velocity and upper plate structures associated with these accreted terranes. The crustal structure of the Kodiak Shelf shows a series of arched reflectors in the lower crust that coincide with low-velocity rocks, providing evidence for large-scale underplating between Kenai Peninsula and Kodiak Island (Moore et al., 1991; Ye et al., 1997). The forearc structure is spatially complex as a result of this accretion history, and may provide important controls on the seismogenic characteristics of megathrust earthquakes, such as their down-dip limit and the seismogenic extent (Kuehn, 2019; Shillington et al., 2022). In the Shumagin segment, the outer forearc has a small frontal prism and hosts active crustal-scale splay faults, indicating a typical tsunamigenic structure (Bécel et al., 2017; von Huene et al., 2021). Downdip variations in the seismic reflection character of the plate interface at the eastern Shumagin segment have been linked to the changes in fault structure and corresponding seismogenic behaviors (J. Li et al., 2015). Along-strike variations in pore-fluid pressure and sediment thickness appear to correlate with changes in seismicity, locking, and earthquake history (J. Li et al., 2018).

The volcanic arc and backarc also show variations between each segment. Active volcanoes are widely distributed along the Alaska Peninsula and the southwestern Alaska Range (Figure 1b). Alaska has about 100 volcanoes active in the past 11,000 years and more than 50 volcanoes considered historically active since 1760 (Cameron et al., 2018). In spatial distribution, both Semidi and Kodiak segments have strong arc volcanism, especially at the arc front of the Kodiak segment. The composition of arc lavas varies along the Alaska Peninsula, which has been attributed to variations in water and sediments entering the subduction zone (Wei et al, 2021). The Bristol Bay Basin, located on the north side of the Alaska Peninsula in the backarc of the Shumagin and Semidi segments, contains a significant thickness of sediments. Active-source studies and numerical models suggest that Bristol Bay formed mainly through two stages. In the early or middle Eocene through a late Miocene phase, extension led to fault-controlled subsidence. Then a late Eocene through Holocene phase of volcanic-arc loading or northward prograding delta led to flexural subsidence (Walker et al., 2003).

Previous passive source seismic studies have mostly investigated the structure of continental portions of southern and central Alaska (Eberhart-Phillips et al., 2006; Qi et al., 2007; Y. Wang & Tape, 2014; Ward, 2015; Martin-Short et al., 2018; Yang & Gao, 2020) or along the Alaska Peninsula (You Tian & Zhao, 2012; Janiszewski et al., 2013). Benefiting from the Earthscope Transportable Array that deployed in Alaska from 2014 until 2021, the entire Alaska region has also been imaged for both isotropic and anisotropic velocity structures (C. Jiang et al., 2018; Ward & Lin, 2018; Feng & Ritzwoller, 2019; Gou et al., 2019; Berg et al., 2020; Feng et al., 2020) as well as seismic velocity interfaces (Gama et al., 2022). However, the lack of seismic array coverage offshore the Alaska Peninsula and the large-scale parameterization of the studies leads to the lack of resolution in the incoming plate and forearc area of the Alaska subduction zone.

Several recent studies have taken advantage of the 2018-2019 AACSE dataset to carry out more detailed studies of the Alaska Peninsula region. A nodal seismograph array installed on Kodiak Island was used to image the structure immediately beneath Kodiak Island (Onyango et al, 2022). Airgun shots recorded by AACSE ocean bottom seismographs provide improved

estimates of shallow crustal structure in the offshore peninsula area (Acquisto et al., 2022a). Body wave tomography (Gou et al., 2022; F. Wang et al., 2022), and surface wave tomography (Feng, 2021; Chuanming Liu et al., 2022) provide improved images of the structure beneath the region. Constraints on azimuthal anisotropy are provided by a recent shear-wave splitting study (Lynner, 2021).

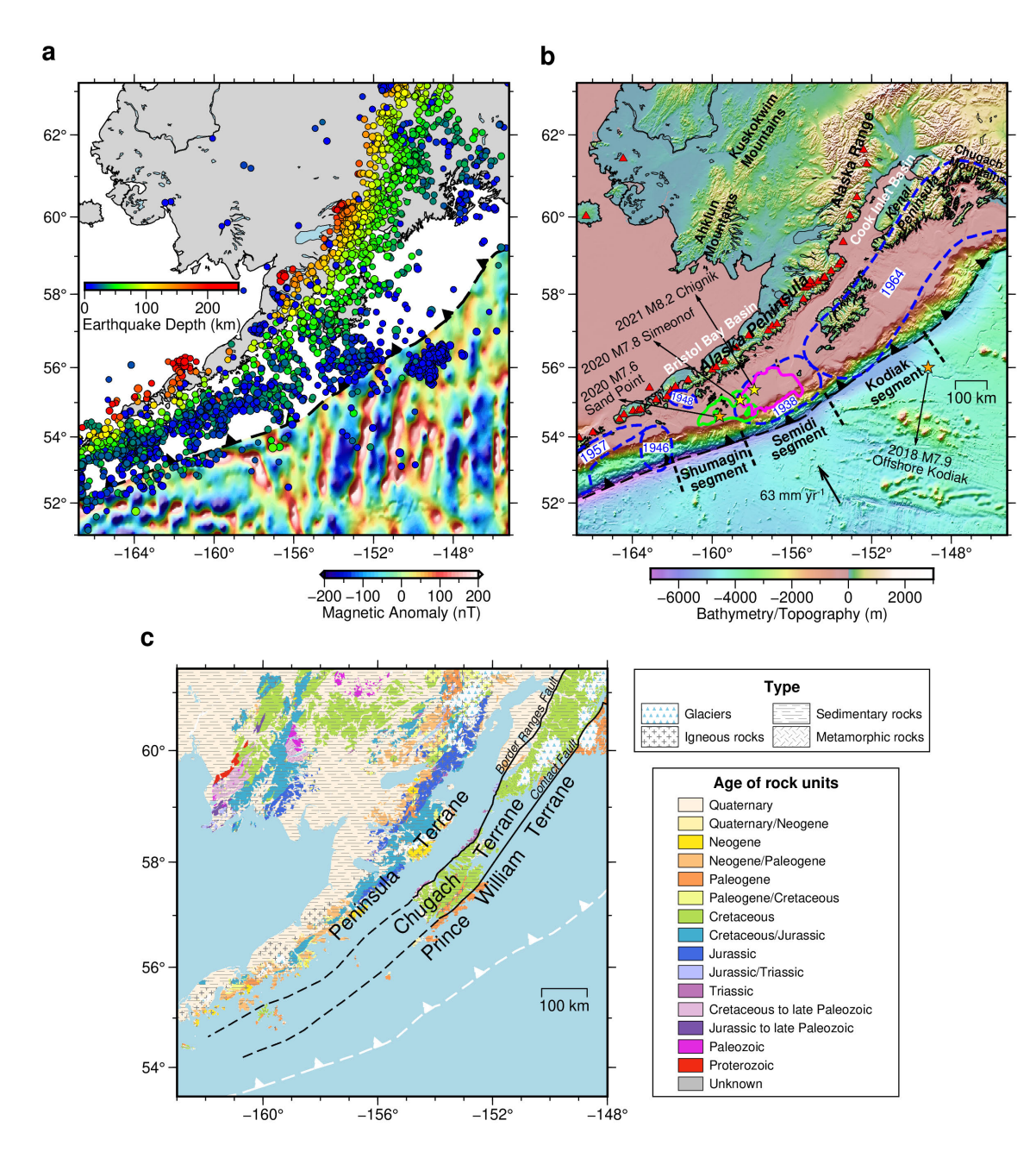


**Figure 1**. The geological setting of the Alaska subduction zone, with the plate boundary marked as the dashed black line with triangles. (a) The magnetic anomaly of the incoming Pacific plate and earthquake distribution. The incoming plate magnetic anomalies are from EMAG2v3 (Meyer

et al., 2017). The earthquakes with  $M \ge 4$  from the Alaska Earthquake Information Center (AEIC) catalog from 1990 to 2022 and from the AACSE catalog during the AACSE deployment (Ruppert et al., 2022) are plotted as circles colored by their epicentral depths. (b) Great earthquake rupture zones and prominent geological regions (e.g., peninsulas, mountains, basins). Dashed blue contours show the rupture zones of historical earthquakes (Davies et al., 1981). Yellow stars indicate the epicenters of megathrust events: the 2020 M7.8 Simeonof earthquake and 2021 M8.2 Chignik earthquake, and their rupture zones are shown as green and magenta, respectively (Liu et al., 2020; Chengli Liu et al., 2022). Orange stars show the epicenters of the 2018 M7.9 Offshore Kodiak earthquake and the 2020 M7.6 Sand Point earthquake, both of which are intraplate strike-slip events. The division of the Shumagin segment, Semidi segment, and Kodiak segment is labeled on the incoming Pacific plate. The convergence rate between the Pacific plate and the North American plate is relatively uniform in the study area, thus a black arrow with the average value (~63 mm yr<sup>-1</sup>) is marked on the incoming plate (DeMets et al., 2010). (c) Locations of the Peninsula Terrane, the Chugach Terrane, and the Prince William Terrane (Horowitz et al., 1989) on the geologic map of the Alaska subduction zone (F. H. Wilson et al., 2015). These terranes have distinctly different rock ages, bounded by the Border Ranges Fault and the Contact Fault, respectively. The well-determined positions of faults are shown as solid lines and locations that are only approximate are shown as dashed lines. 

# **3 Data and Method**

### 3.1 Seismic data

Data for this analysis come from the Alaska Amphibious Community Seismic Experiment (AACSE; May 2018 – September 2019) as well as several land seismograph networks. The AASCE deployed an array of broadband seismic stations covering the Alaska-Aleutian Trench and the Alaska Peninsula from May 2018 to September 2019, including 75 ocean bottom seismographs (OBSs) and 30 land stations (Barcheck et al., 2020). At the same time, the EarthScope Transportable Array (TA) was operating many seismic stations throughout Alaska. Therefore, land stations from TA and several other networks also augment the amphibious seismic array.

After excluding those stations with non-broadband sensors, or poor quality, this study includes 61 AACSE ocean bottom seismographs (OBSs), 30 AACSE land stations, and 179 land stations of other networks (network codes: TA, AK, II, AT, GM, YG, AV) to analyze the Rayleigh wave dispersion. The quality of stations is examined for their long-term noise levels by calculating the Power Spectral Density (PSD) Power Density Function (PDF). Poor-quality stations are those with strange shapes or extreme values in the PSD PDF plots. Altogether, we use a dense amphibious array of 270 seismic stations to perform tomographic inversion (see Section 3.3 to 3.5). In addition, we use 40 land stations that operated outside the AACSE deployment time period for P-wave receiver functions only (see Section 3.6). The detailed distribution of stations that contribute to this study is shown in Figure 2.

Some AACSE land sites on Kodiak Island and the Alaska Peninsula experienced bear attacks on their GPS antennae and lost time synchronization. Some OBSs have possible clock drift due to the early shutdown of their dataloggers and clocks. We test and correct the time drift

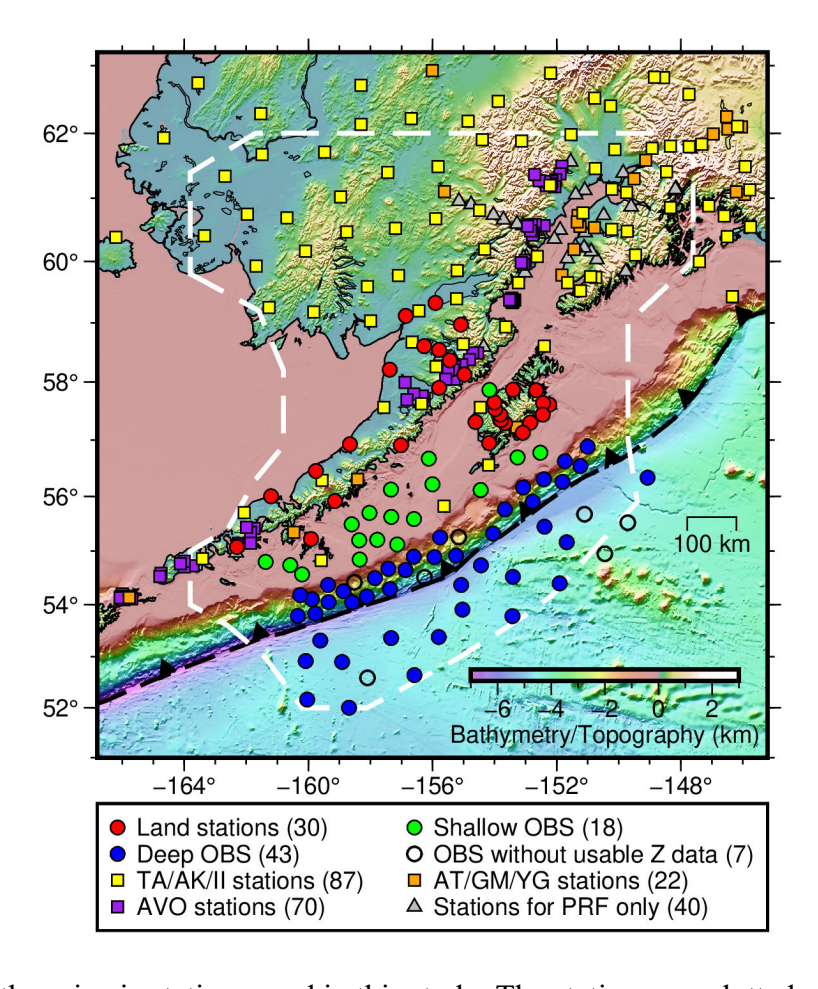


Figure 2. A map of the seismic stations used in this study. The stations are plotted with different shapes and colors according to their networks and types. Red, green, and blue circles represent land stations, shallow ocean bottom seismographs (OBS), and deep OBS, respectively, that were deployed by the AACSE project (Barcheck et al., 2020), OBSs without usable vertical component data are shown as blank circles. Yellow squares are the land stations of the Transportable Array (TA), Alaska Network (AK), and Global Seismic Network. Orange squares are the land stations of the Tsunami Warning, and U.S. Geological Survey Networks (GM). Purple squares are the stations belonging to the Alaska Volcano Observatory (AVO) network, which are clustered around volcanoes. Gray triangles are those stations that are used for receiver function analysis only. Note that the 4 OBSs that were not recovered and 3 OBSs that failed to

record any seismic or pressure data are not included here (Barcheck et al., 2020). The dashed white line encloses the study region defined in Section 3.5.

### 3.2 Pre-processing the OBS data

OBS data usually contain noises that are not present in land seismic records, since the seafloor environment generally has higher noise levels in the long-period seismic band. Previous work has shown that for OBS vertical component data, there are two main noise sources: one is tilt noise resulting from variable ocean-bottom currents tilting the instrument and causing horizontal noise to be recorded by the vertical component; the other is compliance noise resulting from the vertical movements of seafloor due to sea bottom pressure changes resulting from infragravity waves (Webb & Crawford, 1999; Crawford & Webb, 2000). The similarity of tilt noise on vertical and horizontal components, and the similarity of compliance noise on the vertical component and the differential pressure gauge (DPG) suggest that both noises on the vertical component can be largely removed by estimating spectral transfer functions (Bell et al., 2014). For various types of AACSE OBSs, there are three different types of pressure channels: differential pressure gauge (DPG), absolute pressure gauge (APG), and hydrophone. Through tests and comparisons, we found that both DPG and APG are able to remove the compliance noise, while the hydrophone is not very successful.

We use equations 1-7 in Bell et al. (2014) to calculate the spectral transfer function used for noise removal. The transfer functions are best calculated from time series without earthquakes, so we select time windows for transfer function estimation by combining methods described in previous studies (Ye Tian & Ritzwoller, 2017; Janiszewski et al., 2019; Ma et al., 2020). First we predict the arrival time of earthquakes with  $M_S/M_W \ge 4.5$  using the International Seismological Centre (ISC) catalog where the Rayleigh wave time window is taken from 20 s before a predicted 4.0 km s<sup>-1</sup> arrival to 600 s after it, and exclude any time windows that overlap with the Rayleigh wave windows (Ma et al., 2020). Then we check the remaining time windows in an earthquake band (10-40 s) and remove those with suspicious high amplitudes (either small earthquakes or signal singularities). Furthermore, the remaining time windows are then evaluated using a norm outlier rejection method (Janiszewski et al., 2019). In this way, the selected time windows will contain purely noises.

We use the coherence of the transfer function between the vertical and horizontal seismic components as well as the vertical and the pressure time series to determine the frequencies for noise removal. To avoid over-corrections that would distort the signals, we follow Ye Tian and Ritzwoller (2017) and only apply corrections for periods where the transfer function coherence is above 0.4, which mostly lies in a period range between 15 and 150 s. After removing the tilt and compliance noise, the surface wave signals extracted from both ambient noise cross-correlations and teleseismic earthquakes are distinctly improved (Figure S1 in the Supporting Information).

### 3.3 Ambient noise tomography

With the data of all land stations and pre-processed OBSs, the interstation empirical Green's functions are then determined by ambient noise cross-correlation procedures described

in Bensen et al. (2007). First we cut the continuous data to daily length and down-sample them to one sample per second. Then we calculate the ambient noise cross-correlations over the vertical-vertical components of daily length time series using both time-domain normalization with an earthquake filtering band of 10-40 s and spectral whitening. Daily cross-correlations are stacked for each station pair over the entire time period of the deployment.

We then apply an automated Frequency-Time Analysis (FTAN) with a phase-matched filter to measure the Rayleigh wave phase and group velocity dispersion curves from the symmetric Green's functions of each station pair (Bensen et al., 2007; Lin et al., 2008). The FTAN method directly measures group velocity dispersion, but requires reference phase velocity dispersion curves to avoid cycle-skipping problems in determining the phase velocity dispersion. To avoid the cycle-skipping problems, we use a two-step process similar to Lin et al. (2008): (1) We apply FTAN using the reference interstation phase velocity dispersion curves from global Rayleigh wave dispersion model GDM52 (25-250 s) (Ekström, 2011), resulting preliminary measurements where most station pairs have resolved the cycle-skipping problems. Using the tomographic method and selection criteria described below, we invert for preliminary phase velocity maps at periods between 8 and 36 s. We use these maps to estimate the dispersion curves for every station pair which we then use as the revised reference curves. (2) We repeat the FTAN using the revised reference interstation phase velocity curves, resulting all interstation measurements without cycle-skipping problems. As there are rapid changes from oceanic to continental structures, the FTAN measurements for land-land station pairs, OBS-land station pairs, and OBS-OBS pairs also vary a lot (Figure S2 in the Supporting Information). The oceanic paths generally show extremely low group/phase velocity at periods < 16 s but increase rapidly to high velocity at periods > 20 s.

To quantify the strength of signals for each station pair, we define the frequency-dependent signal-to-noise ratio (SNR) as the ratio of the signal peak in the predicted arrival window to the root mean square (rms) of the noise trailing the arrival window, in each period band for the symmetric component cross-correlation. The prediction window is defined by assuming surface waves travel between 0.5 and 5.0 km/s, and the trailing noise window starts 500 s after the predicted window until the end of lag time. There are relatively few good measurements below 8 s, and the SNR decreases rapidly for oceanic paths at periods greater than 36 s, thus we invert for phase and group velocity maps from 8 to 36 s using a Gaussian ray-theoretical tomography method (Barmin et al., 2001). The grid spacing is  $0.3^{\circ} \times 0.2^{\circ}$ , which is roughly equally spaced in longitude and latitude. The isotropic cell size in the tomographic inversion is  $0.5^{\circ}$ , which could recover checker sizes ranging from  $3^{\circ} \times 2^{\circ}$  to  $1.8^{\circ} \times 1.2^{\circ}$  in checkerboard tests (Figure S3 in the Supporting Information).

For each frequency, we only keep station pairs with distances larger than twice the wavelength. To exclude the unreliable measurements while considering the relatively high noise of OBS records, we excluded measurements with SNR < 7. To further constrain the 2-D inversion results, we apply quality control based on the travel-time residuals from the previous inversion. The paths with residuals outside two standard deviations, about 2 % to 6 % of the total measurements for each period, are removed after three times of quality control. The remaining measurements are used to finalize the Rayleigh phase and group velocity maps from 8 s to 36 s (Figure S4 in the Supporting Information). At short periods (between 8 to 14 s), the group and phase velocity maps reflect the very shallow structure and water depth, where incoming plate and trench are dominated by low-speed anomalies and mountain ranges show high-speed

anomalies. At longer periods (20-30 s), the group and phase velocity maps reflect the crust and uppermost mantle structure, where the incoming plate is dominated by high-speed anomalies and low-speed anomalies cover the forearc region.

## 3.4 Teleseismic earthquake tomography

At longer periods (T > 20 s), we analyze the Rayleigh wave phase velocity from teleseismic waves traversing the array using the Helmholtz tomography method (Lin & Ritzwoller, 2011) implemented in the ASWMS package (Jin & Gaherty, 2015). We select earthquakes with  $M_W \geq 5$  and epicentral distances between  $20^\circ$  and  $160^\circ$  from the International Seismological Centre (ISC) catalog for analysis. The events are chosen to be high-quality, relatively evenly distributed with respect to the seismic array, and also separated enough in time from each other to avoid overlapping on seismograms. High-quality events refer to those that pass the automatic quality control in the ASWMS package based on the coherence of nearby stations and reasonable misfit in the Eikonal and amplitude inversions. Finally, 265 earthquakes are used to determine the phase velocities.

The implementation of Helmholtz tomography involves Eikonal tomography plus the amplitude term correction, where Eikonal tomography inverts the phase delays for spatial variations in apparent phase velocity via the Eikonal equation (Lin et al., 2009) and amplitude Laplacian term correction accounts for the local amplification due to wavefield focusing and defocusing effects (Lin et al., 2012; Eddy & Ekström, 2014; Russell & Dalton, 2022). The amplitude term corrects for the influence of non-plane wave propagation on the apparent phase velocities, allowing for the recovery of the true structural phase velocity via the Helmholtz equation. The waveforms of all events and stations are cut from the earthquake origin time to 10800 s after. Based on multichannel cross-correlations of station pairs within 410 km, the phase velocity variations of a series of periods are estimated for each event at node spacing  $0.3^{\circ} \times 0.2^{\circ}$ . We estimate the local amplification term (Eddy & Ekström, 2014), calculate the smoothed Laplacian term of corrected 2-D amplitudes, and finally convert the apparent phase velocity to structural phase velocity for each period. The final structural phase velocity dispersion maps are stacked over maps of all events. The checkboard tests show that the inverted velocity maps show distinct checkers and generally recover more than 80% of input anomaly amplitudes, suggesting that the parameters above work well (Figure S5 in the Supporting Information).

The tomographic results produce isotropic phase velocity at node spacing  $0.3^{\circ} \times 0.2^{\circ}$  for periods from 23 s to 100 s (Figure S6 in the Supporting Information). The phase velocity maps at these longer periods constrain the lower crust and uppermost mantle structure. At the 40 s period, the high-velocity anomalies still dominate the incoming plate region, and also extend north across the Aleutian Trench a little bit compared to the 25 s phase velocity map. At even longer periods (e.g., 60 s, 100 s), the trench region is replaced by low velocity, and high-speed anomalies gradually occupy the volcanic arc.

### 3.5 Local Rayleigh wave dispersion curves

The Rayleigh wave phase velocity dispersion curves measured from ambient noise and earthquake data are then evaluated in their overlapping period band. The study region is defined by the areas that are well-recovered in checkerboard tests of both ambient noise tomography and teleseismic earthquake tomography. Comparisons between the phase velocity maps show that

# manuscript submitted to Journal of Geophysical Research: Solid Earth

389	their measurements are generally consistent at 24-34 s periods. For example, at 30 s, most of the
390	phase velocity differences are less than 0.1 km s <sup>-1</sup> (Figure 3). The incoming plate, trench, and
391	northern Bristol Bay area generally have slightly higher phase velocity from ambient noise
392	tomography than from earthquake tomography, whereas other areas show the opposite
393	relationship (Figure 3). Furthermore, we define the reliable range of nodes to extract local
394	dispersion curves as those with high ray path coverage in both ambient noise tomography and

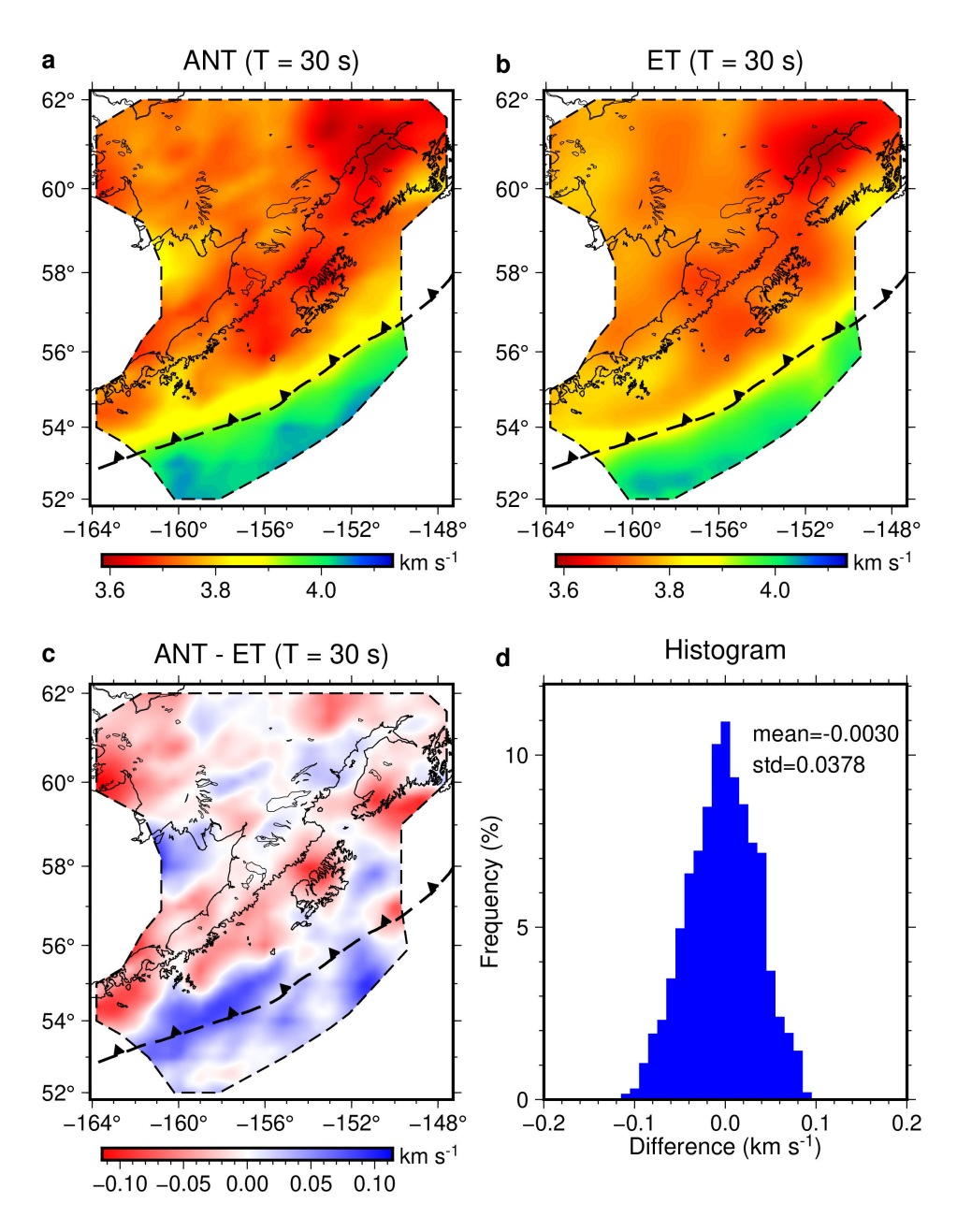


**Figure 3**. Comparison of Rayleigh wave phase velocity at 30 s period of the study region estimated from ambient noise tomography (ANT) and earthquake Helmholtz tomography (ET). (a) The phase velocity map at 30 s from ANT. (b) The phase velocity map at 30 s from ET. (c) The difference between phase velocity maps from ANT and ET at 30 s. (d) Histogram of the

differences in (c), showing that the results from the two tomography results are generally less than 0.1 km s<sup>-1</sup>.

Therefore, the final phase velocity dispersion curves for each node are constructed in the following way: 1) For periods less than or equal to 23 s, the phase velocities come from ambient noise tomography. 2) For periods greater than or equal to 36 s, the phase velocities come from Eikonal tomography. 3) For periods larger than 23 and less than 36 s, we take a weighted average of the measurements from the two methods, with the weights changing linearly in between.

Uncertainty estimation of the local phase and group velocity curves is important for the shear velocity inversion. The tomographic methods used here do not provide an estimation of uncertainties directly, but we can estimate the local uncertainties for short periods from the local resolution in the method of Barmin et al. (2001). Similar to Shen et al. (2016), we use an empirical scaling relationship:

$$\sigma(\mathbf{r}) = kR(\mathbf{r}) \tag{1}$$

where  $\sigma(\mathbf{r})$  is the uncertainty estimate at location  $\mathbf{r}$ , and  $R(\mathbf{r})$  is the estimate of resolution, which is the standard deviation of the resolving kernel at the location (Barmin et al., 2001). We estimate the value of k for each period, so that a local resolution of ~50 km (i.e., minimum resolution value in the data-rich region) produces a phase velocity uncertainty estimate of 0.027 km s<sup>-1</sup> for 8 s, 0.021 km s<sup>-1</sup> for 16 s, 0.016 km s<sup>-1</sup> for 24 s, 0.021 km s<sup>-1</sup> for 32 s, 0.024 km s<sup>-1</sup> for periods > 32 s. Uncertainties for other periods are interpolated based on these anchor points. From an empirical relationship, the uncertainties of group velocity are estimated to be twice that of phase velocity (e.g., Moschetti et al., 2010; Shen et al., 2016). Considering that the group velocity measurements in this region have even larger uncertainty at shorter periods, we use a factor of 2.5 to calculate the group velocity uncertainties. The local uncertainties of phase velocity from the Helmholtz tomography are scaled from the corresponding standard deviation values by multiplying a factor of 0.3. In this way, the phase velocities from two datasets at overlapped periods have similar uncertainties.

### 3.6 P-wave receiver functions for land stations

Contrasting to the surface wave analysis that requires a concurrent deployment of seismic stations, the P-wave receiver functions (PRFs) analysis is performed on each station individually. To use joint inversion to better constrain the continental Moho, we try to include all land stations within the study region that operated sufficient dates from May 2014 to December 2021. The longer date range is chosen to make the best use of TA stations and other temporary stations with enough data outside the AACSE deployment period. For all land stations with sufficient data quantity and quality, we first prepare the P-wave seismic data from earthquakes with  $m_b \ge 5.0$  and epicentral distances between 30° and 90°. The seismograms are decimated to a sample rate of 10 Hz and cut to a time window from 30 s before and 60 s after the P-wave onset. The horizontal components are cosine tapered and pre-filtered with a bandpass filter of 0.02 to 2 Hz, then rotated into radial and transverse components. Using a time-domain iterative deconvolution

algorithm (Ligorría & Ammon, 1999), we perform 200 iterations to estimate the PRFs, using a Gaussian low pass filter with a corner frequency of ~1 s.

We apply automated quality control to the PRFs in two steps. First we correct the time to align the Ps phase and check individual PRFs to exclude those problematic ones (e.g., extreme amplitude, negative polarity at t = 0). Then we use the similarity of PRFs over the range of back-azimuths to further constrain the quality and generally retain more than 30 PRFs for each station. If the individual PRFs have good azimuthal coverage, a "harmonic stripping" method is applied to determine the isotropic or average PRF, which represents the common component over all azimuths (Shen et al., 2013). For stations lacking a good azimuthal distribution of individual PRFs, we use a weighted stack of all PRFs to get a single PRF for the station site. In total, we obtain 188 land stations with quality-controlled stacked PRFs. The stacked PRFs of stations along profiles suggest that the overall quality of the PRFs is reasonably good to constrain the interface structures (Figure S7 in the Supporting Information).

## 3.7 Bayesian Monte Carlo inversion

The resulting local Rayleigh wave dispersion curves with group velocity from 8-36 s and phase velocity from 8-100 s are then inverted for the azimuthally averaged vertically polarized shear wave velocity ( $V_{SV}$ ) structure using a Bayesian Monte Carlo inversion method (Shen et al., 2013; Shen & Ritzwoller, 2016). The Bayesian inversion requires the proper construction of the model space and the estimation of prior information, which is based on the location of the nodes. We divide the nodes into three groups: the incoming plate group to the south of the trench axis, the inner trench slope group just north of the trench axis, and the forearc and backarc group. The boundary between the inner trench slope and the forearc/backarc region is taken as the 20 km depth contour of the slab interface from the Slab2.0 model (Hayes et al., 2018).

For the nodes in the ocean, we include a water layer with a starting thickness from the 125-km Gaussian-filtered bathymetry (m<sub>w0</sub>) and allow a 100% thickness but no more than 1.5 km perturbation. The incoming plate nodes include a 0-1 km sedimentary layer in the Shumagin segment and a 0-2 km sedimentary layer in the Semidi and Kodiak segments, based on the previous active-source results (Shillington et al., 2015). For inner trench nodes, the starting crustal thickness of (m<sub>c0</sub>) is calculated following the depth of slab interface as well as the slab dip angle in the Slab2.0 model, with an assumption of a 6 km oceanic crust atop the subducting slab. The crustal thickness of most nodes in the inner trench slope region then allows a 30% thickness perturbation with respect to m<sub>c0</sub>. One exception is the Kenai Peninsula nodes, which have a slab interface less than 20 km in the Slab2.0 model, but tend to have a deeper Moho than that predicted by the slab interface through tests. We thus allow those nodes within the Kenai Peninsula to have a 60% thickness perturbation with respect to m<sub>c0</sub>. For all nodes, the uppermost mantle structure from the Moho discontinuity down to 300 km depth is represented by a 6-knot B-spline curve. The bottom 100 km is gradually merged into the STW105 V<sub>SV</sub> model (Kustowski et al., 2008). The parameterization and search range of the velocity models in different regions are defined by a series of variables for three groups of nodes (Table 1). Each

variable in different regions is set accordingly based on our a priori information of the study region.

Table 1. Parameterization and search range for the velocity models in different regions.

		Incoming plate	Inner trench slope	Forearc and backarc
Water layer (for oceanic nodes only)	Thickness	$m_{w0} \pm min(m_{w0}, 1.5)$ (km)		
Sedimentary layer	Thickness	Shumagin: 0-1 km Semidi & Kodiak: 0-2 km	0-6 km	0-6 km
	V <sub>SV</sub> (top: 1.0 km s <sup>-1</sup> ; bottom: 2.0 km s <sup>-1</sup> )	Linear velocity increase, with top and bottom allows 1.0 km s <sup>-1</sup> and 1.5 km s <sup>-1</sup> perturbation, respectively		
Crustal	Thickness	4-8 km	For nodes within Kenai Peninsula: $m_{c0} \pm 0.6 \ m_{c0} \ (km)$ For others: $m_{c0} \pm 0.3 \ m_{c0} \ (km)$	20-50 km
layer	V <sub>sv</sub> (top: 3.1 km s <sup>-1</sup> ; bottom: 3.8 km s <sup>-1</sup> )	Linear velocity increase, both variables allow 20% perturbation	3 cubic B-spline coefficients, each allows 20% perturbation	4 cubic B-spline coefficients, each allows 20% perturbation
Mantle layer	V <sub>sv</sub> (top: 4.2 km s <sup>-1</sup> ; bottom: 4.4 km s <sup>-1</sup> )	6 cubic B-spline coefficients, each allows 25% perturbation		

The Bayesian Monte Carlo inversion is performed with a grid of  $0.3^{\circ} \times 0.2^{\circ}$  spaced nodes which have phase and group velocity measurements from both ambient noise data and teleseismic earthquake data. Examples of inversion results show that the Bayesian Monte Carlo inversion can well fit the measured group and phase velocity dispersion curves (Figure 4a;

Figure 4b). Finally, all 2015 evenly spaced nodes give structures that are based on the mean of at least 5000 acceptable models.

For land stations with high-quality PRFs, their local structures at stations are jointly determined using the Rayleigh wave dispersion and PRFs. The Moho conversion in the PRF between 3 and 7 s is very helpful to invert the Moho depth and resolve potential trade-offs between Moho depth and velocity structure (Figure 4c), so we fit the first 10 s of the PRFs. Among all 188 stations with high-quality PRFs, we finally get 180 well-constrained joint inversion results and their structures are generally based on the mean of at least 500 acceptable models. The joint inversion requires fewer accepted models to achieve meaningful and stable results since the receiver function helps reduce the model space that fits the datasets. The 3-D structural model is constructed on the grid of evenly spaced nodes by combining the structure from the Rayleigh wave inversion with the PRF joint inversion results for all well-constrained stations within a 75 km distance, using an inverse distance weighting scheme (Shen et al., 2018). The structure for nodes lacking nearby land seismographs with good PRF results is based solely on the Rayleigh wave inversion results. The final 3-D azimuthally-averaged vertically-polarized shear velocity model is determined using all the well-constrained nodes by interpolating with a simple kriging algorithm (Shen & Ritzwoller, 2016; Shen et al., 2018).

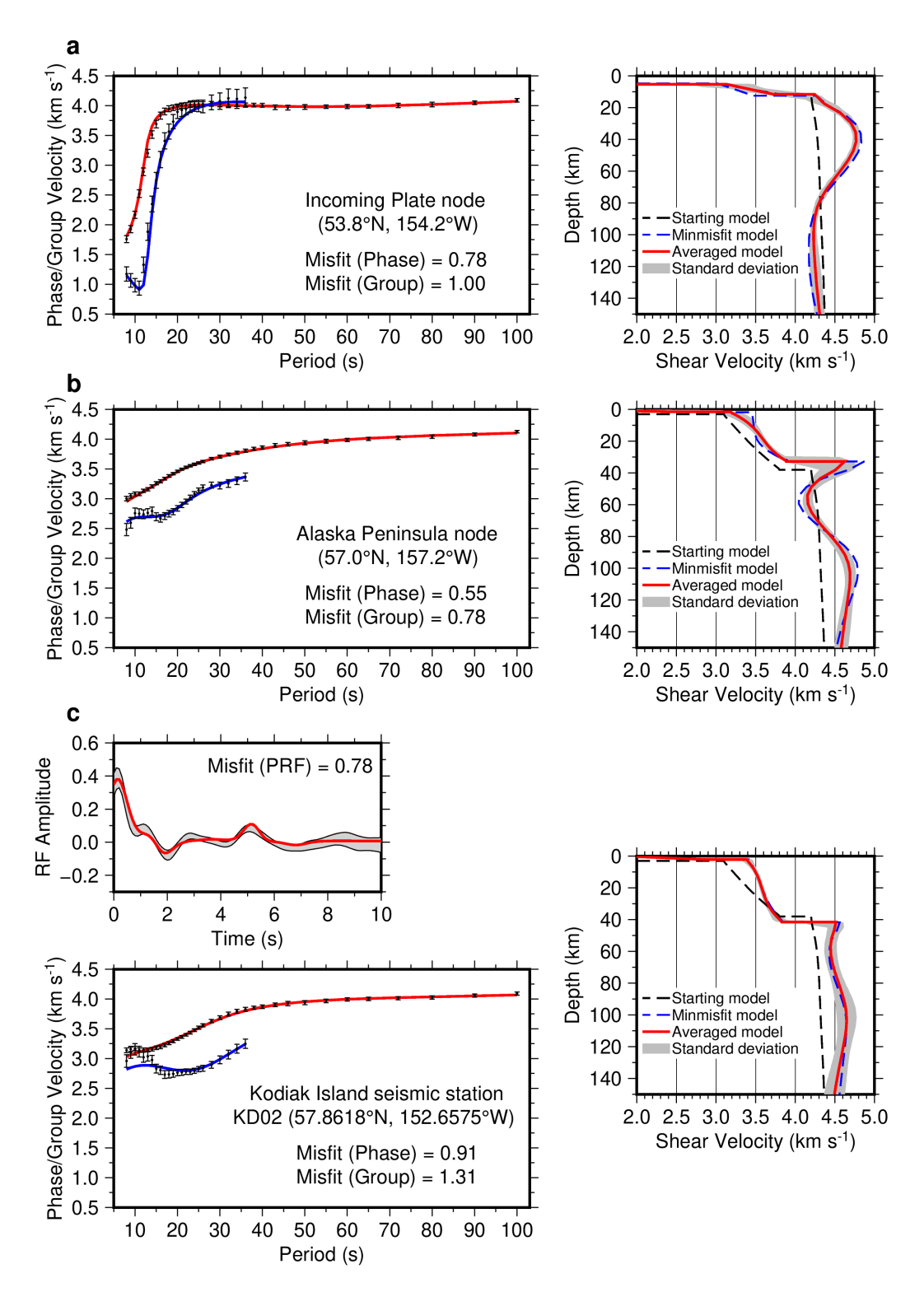


**Figure 4**. Examples of the Bayesian Monte Carlo inversion for different geological regions show the resulting 1-D shear wave velocity structure beneath each node and how the predicted phase and group dispersion curves (and receiver function, if applicable) fit the measurements. (a)

- Incoming plate node (53.8°N, 154.2°W). The derived V<sub>SV</sub> profile is an oceanic structure with
- reduced velocity in the uppermost mantle. (b) Alaska Peninsula node (57.0°N, 157.2°W). The
- derived V<sub>SV</sub> profile is a typical volcanic arc structure with a low-velocity zone (LVZ) beneath
- the Moho. (c) Joint inversion result for Kodiak Island seismic station KD02. The structure shows
- a thick, low-velocity crust and a strong subducting oceanic Moho discontinuity.

519

520

521522

523

524

525

526

527

528

529

530

531

532

533

534

535

536

537

538

539

540

541

542

543

544

545

546

547

548

549

550

551

#### 4 Results

### 4.1 Thickness of crust and sediment

The posterior distribution of the crustal thickness and sediment thickness provides their preferred values and uncertainty maps (Figure 5). Note that the inner forearc structure is rather complex as there are possibly two Moho discontinuities (an overriding plate Moho and a subducting plate Moho), but we only set one Moho in the parameterization since the resolution of the methods does not allow for reliably determining a complex structure. The inversion generally picks the shallowest Moho. Therefore, the observed Moho in the seaward part of the forearc represents the subducting plate Moho and the observed Moho in the arcward section of the forearc represents the overriding plate Moho, with a section in between where the overriding and subducting Mohos are in close proximity and the identity of the Moho discontinuity from the inversion is uncertain. The thickest crust is a band in the inner forearc from the Kodiak segment to the eastern edge of the Shumagin segment, whose crustal thickness exceeds that in the arc and backarc regions (Figure 5a). The comparison between the final uncertainty map and that from surface wave inversion only (Figure S7 in the Supporting Information) clearly shows how the PRFs help reduce uncertainty (Figure 5b; Figure S7b). The crustal thickness along the arc is relatively constant (32-36 km) to the west of the Alaska Range (>40 km), slightly thinner than indicated by a previous receiver function analysis of the stations along the Aleutian arc mostly west of the study region (Janiszewski et al., 2013).

Sediment as defined in this study includes both recent pelagic and terrigenous sediment as well as deformed and potentially older sediments in forearc basins and in the accretionary prism. The mean distribution of sediment thickness is generally less than 2 km in the incoming plate and the continental regions. Though the inversion method is not highly sensitive to thin sedimentary cover, the model clearly resolves thicker sediment along the outer forearc of the Kodiak and Semidi segments and in the Bristol Bay and Cook Inlet basins. The very thick (up to 4.5 km thickness) low-velocity sediments in the outer forearc basin (Figure 5c) are consistent with the outer forearc basin structure in the Shumagin segment (Shillington et al., 2022) and to the south of Kodiak Island (Fisher & von Huene, 1982) determined using active source methods, though thickest sediments of Shillington et al. (2022) are in the accretionary prism. Bristol Bay Basin and the Cook Inlet Basin both show about 3 km of low-velocity sediments. The distribution of sediment thickness in the Cook Inlet Basin has a similar pattern to the map of depth to the base of Cenozoic strata (Shellenbaum et al., 2010; Silwal et al., 2018). The previous active-source survey in Bristol Bay Basin shows a boundary at about 3 km depth for the faulted basement (Walker et al., 2003), consistent with the sediment thickness results here.

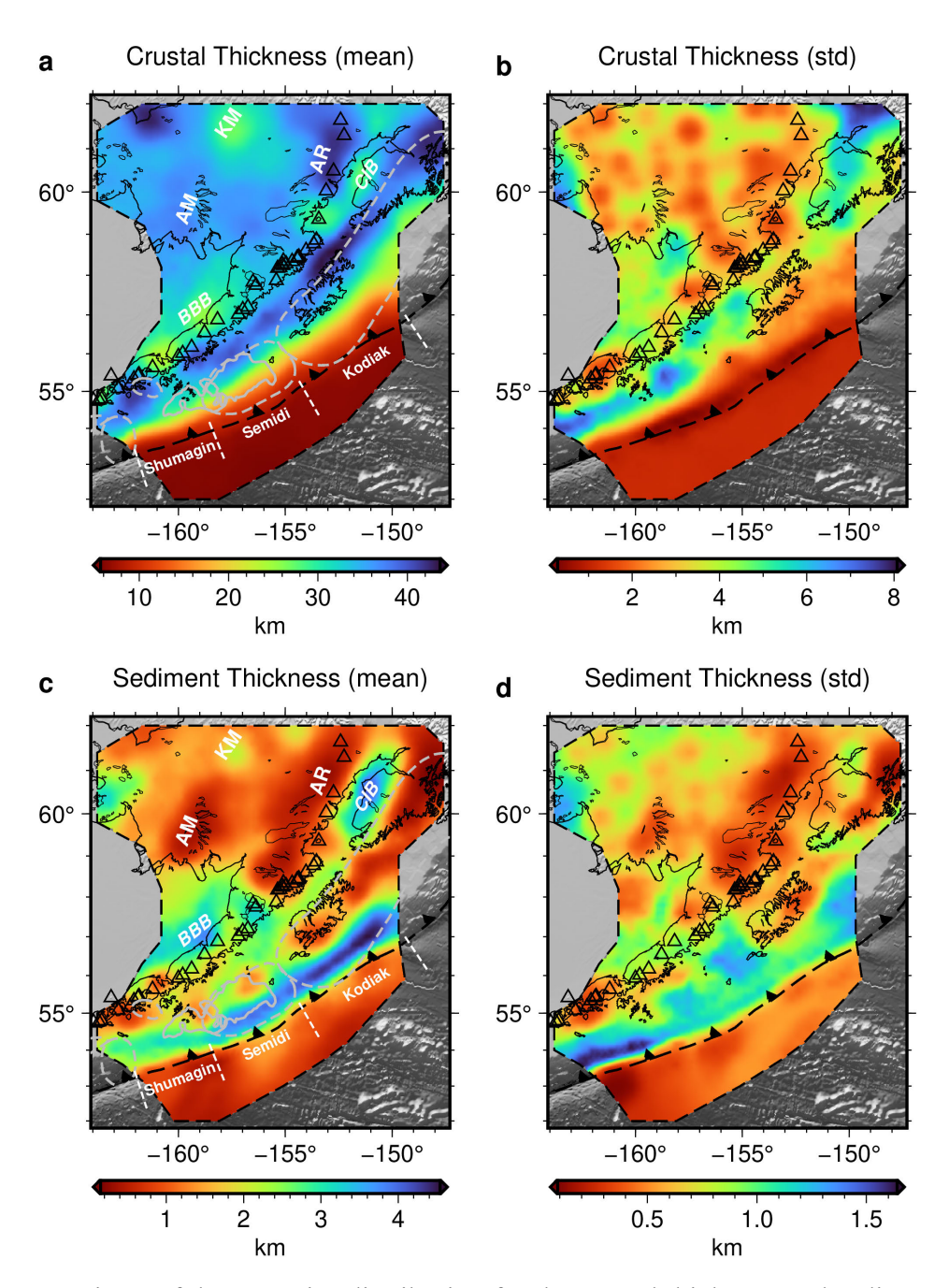


**Figure 5**. Map views of the posterior distribution for the crustal thickness and sediment thickness of the study region. The background image is the topography/bathymetry in gray scales. (a) Map view of the mean of the crustal thickness. The dashed gray lines are the contours of earthquake rupture zones shown in Figure 1b. The dashed white lines marked the range of the Shumagin, Semidi, and Kodiak segments. Annotation of geological features: AM = Ahklun Mountains; KM = Kuskokwim Mountains; AR = Alaska Range; BBB = Bristol Bay Basin; CIB = Cook Inlet Basin. (b) Map view of the uncertainty of the crustal thickness. (c) Map view of the mean of the sediment thickness. Other labels are the same as that in (a). (d) Map view of the uncertainty of the sediment thickness.

## 4.2 Shear velocity structure

 The shear wave velocity structure is presented as a series of map views (Figure 6) as well as cross-sections normal to the trench along the Shumagin, Semidi, and Kodiak segments (Figure 7). The downgoing Pacific plate, featured by high velocity in the mantle, dominates the shear velocity model. The depth of the slab interface changes from less than 10 km near the trench to greater than 100 km beneath the volcanic arc, similar to the slab geometry from previous studies (e.g., Abers et al., 2017). The uppermost mantle beneath the incoming plate shows a clear velocity reduction from the seaward end to the near-trench region (Figure 7).

The 3-D shear velocity model successfully resolves features like the accretionary prism, forearc crust, shallow basins, arc volcanic magma, and major mountains. At very shallow depths (~5 km), the outer forearc is dominated by low-velocity sediment of the accretionary prism while most regions show a typical crystalline upper crust (Figure 6). In the Semidi and Kodiak segments, the outer forearc shows a low-velocity (~3.5 km/s) lower crust with a larger thickness, which is not found in the Shumagin segment. A very similar contrast is also seen in recent active-source imaging, where results show a lower velocity crust in the Semidi segment than that in the Shumagin segment (Burstein et al., 2022). The Bristol Bay Basin is featured by thinner crust, high-velocity lower crust, and low-velocity upper mantle. The low-velocity anomalies beneath volcanic arcs are observed for all segments but are most prominent in the Kodiak segment (Figure 7). The Ahklun Mountains and Kuskokwim Mountains show similar crustal velocities but quite different Moho depths and upper mantle structures (Figure 5; Figure 7).

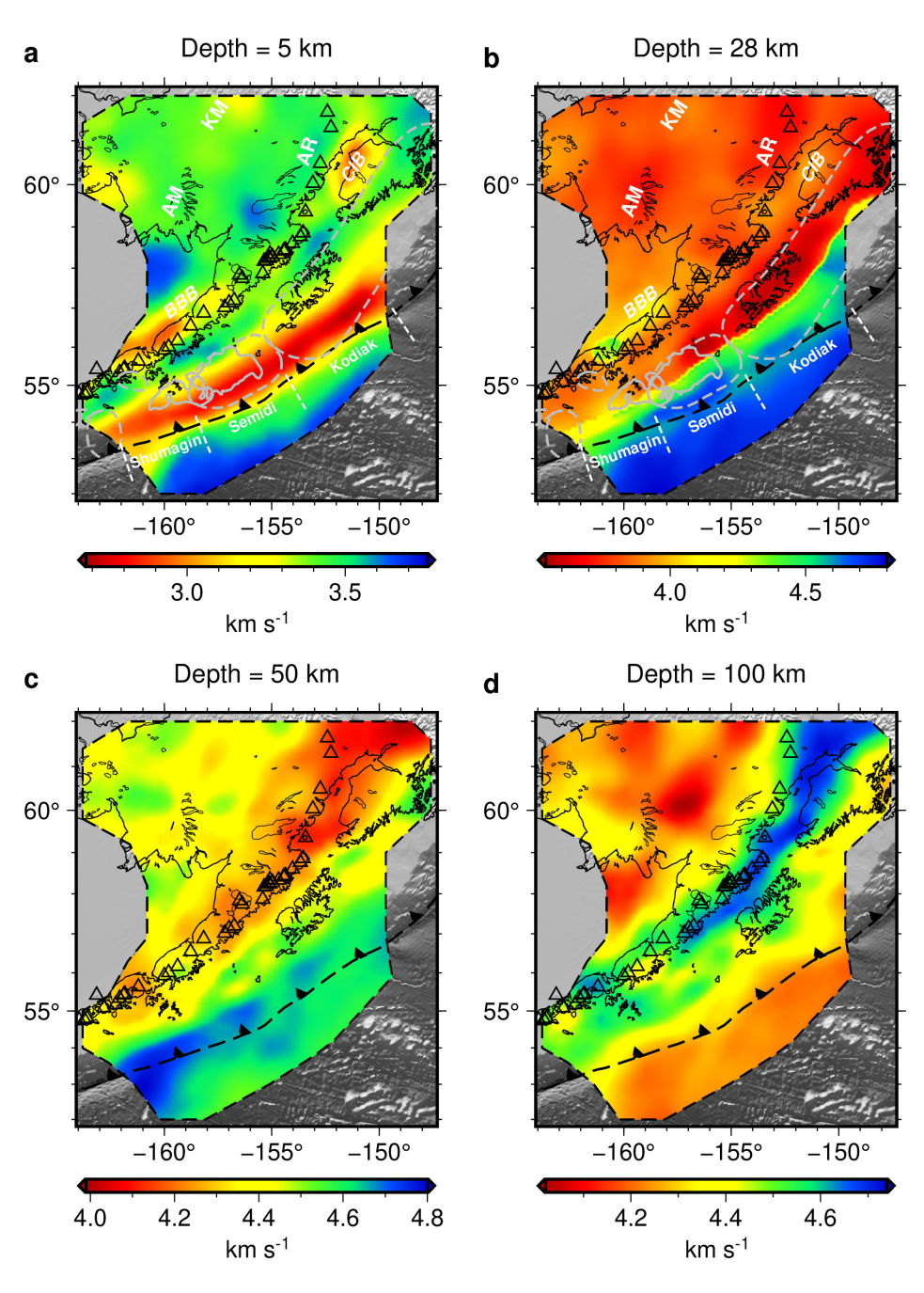


**Figure 6**. Horizontal slices for azimuthal averaged shear wave velocity ( $V_{SV}$ ) of the study region at different depths. The background image is the topography/bathymetry in gray scales. (**a-d**) Map view of the shear velocity at 5, 28, 50, and 100 km depths, respectively. The depth is defined here as relative to the solid surface, either the seafloor or the continental surface. Active volcanoes are marked as triangles along the volcanic arc. Note that there are different velocity color scales for each sub-figure. In (a) and (b), the dashed gray lines are the contours of earthquake rupture zones shown in Figure 1b and the dashed white lines marked the range of Shumagin, Semidi, and Kodiak segments. Annotation of geological features: AM = Ahklun Mountains; KM = Kuskokwim Mountains; AR = Alaska Range; BBB = Bristol Bay Basin; CIB = Cook Inlet Basin.

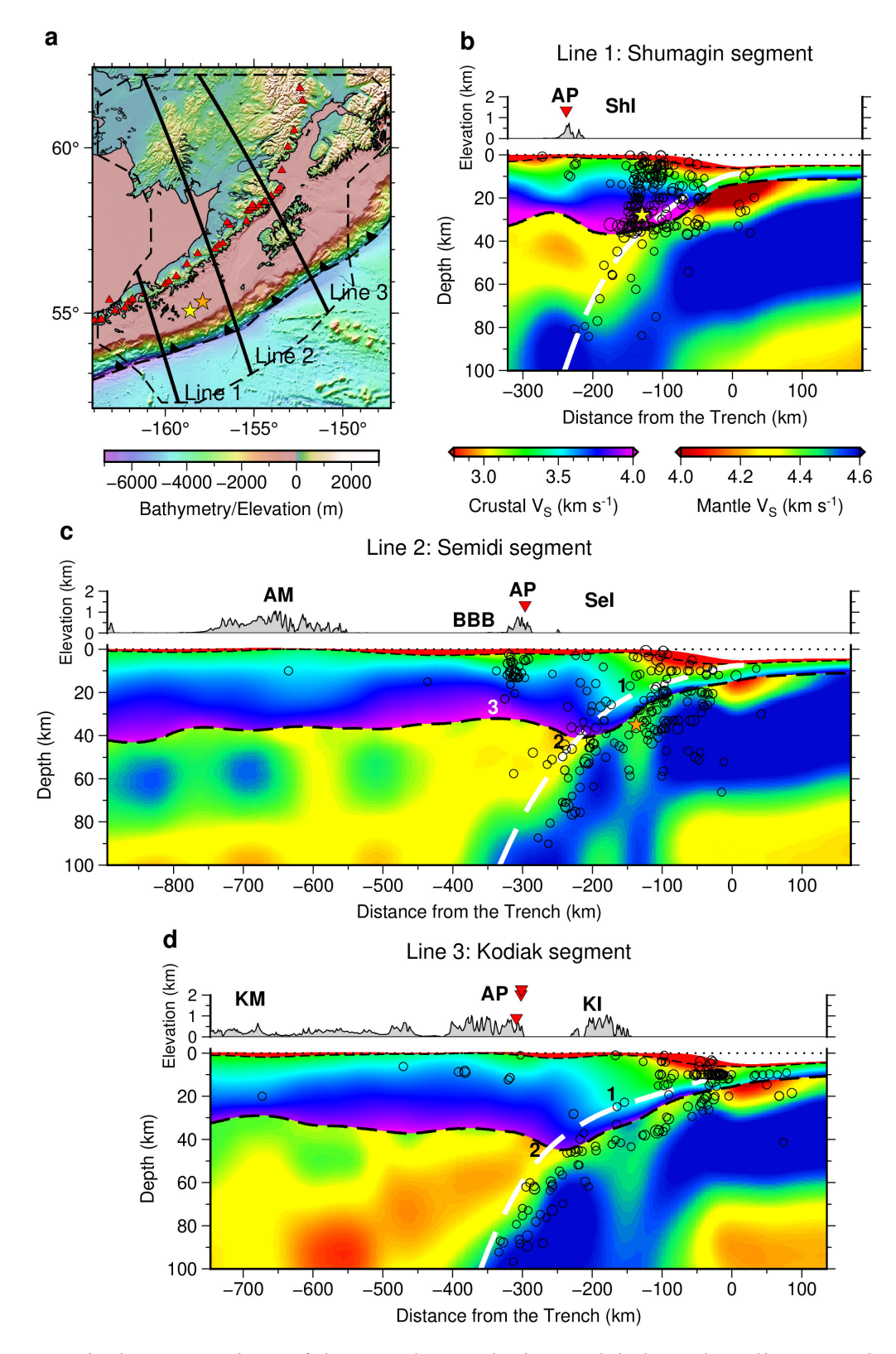


**Figure 7**. Vertical cross-sections of the 3-D shear velocity model along three lines crossing the Shumagin, Semidi, and Kodiak segments, respectively. (a) Location of the three lines shown on

the bathymetry and elevation map. The arc volcanoes are plotted as red triangles. The epicenter 601 602 of the 2020 M7.8 Simeonof megathrust earthquake (~28 km depth) is marked by a yellow star. The epicenter of the 2021 M8.2 Chignik megathrust earthquake (~35 km depth) is marked by an 603 orange star. The dashed black line encloses the study region. (b-d) Cross-sections along each 604 line. The x-axis is the distance relative to the trench axis with a positive distance in the direction 605 of the incoming Pacific plate. The elevation along the profile is plotted above the velocity image 606 with geological features labeled (Annotation: AP = Alaska Peninsula; AM = Ahklun Mountains; 607 KM = Kuskokwim Mountains; BBB = Bristol Bay Basin; ShI = Shumagin Islands; SeI = Semidi 608 Islands; KI = Kodiak Island). Active volcanoes near the profiles (within 25 km) are plotted as red 609 triangles, above the topography image. The V<sub>SV</sub> images show the structure along each cross-610 section, where V<sub>SV</sub> values in the crust and mantle use different color bars. Depths are plotted 611 relative to sea level here (shown as a black dotted line). The thin black dashed line is the 612 boundary between sediment and crust, while the thick black dashed line is the Moho depth in the 613 3-D V<sub>SV</sub> model. The white dashed line depicts the depth of the slab interface from Slab2.0 614 (Hayes et al., 2018). The  $M \ge 4$  earthquakes from the AEIC catalog since 1990 and the AACSE 615 catalog (Ruppert et al., 2022) are plotted on the cross-section image as open black circles if they 616 are within 50 km from the projection line. The hypocenter of the 2020 M7.8 Simeonof 617 megathrust event is projected to the cross-section along Line 1 and shown as a yellow star in (b). 618 The hypocenter of the 2021 M8.2 Chignik megathrust event is projected to the cross-section 619 along Line 2 and shown as an orange star in (c). Labels 1, 2, and 3 are for reference of some 620 velocity features discussed in the text. 621

### 5 Discussion

622

623

624

625

626 627

628

629 630

631

632

633

634

635

636

637

638

639

640

641 642

643

The 3-D shear velocity images clearly reveal systematic along-strike variations in the subduction zone structure. Here we will focus on the predominant features, discussing the forearc crustal thickness, the backarc basin structure, and the incoming plate hydration.

#### 5.1 Thick forearc crust associated with the Chugach Terrane

The crustal structure of the forearc shows a band of thick crust (35-42 km) extending from the eastern edge of the study region, beneath Kodiak Island, to just east of the Shumagin Islands. Crustal thickness in this region generally exceeds the crustal thickness of the volcanic arc and backarc regions (Figure 5a). Immediately seaward of the thickest crust, the velocity profile is characterized by a thick section of reduced lower crustal velocities (~3.5 km s<sup>-1</sup>) extending to the plate interface at depths of about 30 km at many locations (label 1 in Figure 7c and Figure 7d). This feature may be the along-strike continuation of the 20-km-thick low velocity lower crustal units imaged just to the east of Kodiak Island by the EDGE active source study (Ye et al., 1997). The shear velocities in this study are consistent with the lowermost crustal P wave velocity of about 6.0 km s<sup>-1</sup> observed by Ye et al. (1997). They interpreted the low-velocity region as underplated sediments and upper crustal rocks of subducted terrains, associated with the uplift of the Kodiak region during the Eocene to Oligocene (Moore et al., 1991). An alternative interpretation is that those lower velocities represent the Paleogene-aged Prince William Terrane and/or the Mesozoic-aged Chugach Terrane (e.g., Horowitz et al., 1989) (Figure 1c); these terranes are dominantly composed of lightly metamorphosed accretionary complexes (e.g., Sample & Moore, 1987), which would also be expected to have relatively low

velocities. In this case, the reflections observed by Moore et al. (1991) may arise from layering within Prince William/Chugach/Peninsula Terranes from accretionary complexes or intrusions (Figure 1c). Intracrustal reflections are observed on all the Alaska/Aleutian arc profiles and bright bands of lower crustal reflections are even observed farther west in the oceanic part of the arc (Calvert & McGeary, 2013). However, these studies did not show a clear anticlinal structure as described by Moore et al. (1991) and Ye et al. (1997).

The results presented here suggest that the distinctive thickened crust just inboard of the slow lower crustal forearc material extends to the eastern edge of the Shumagin Islands region. The Chugach Terrane is often thought to extend to Sanak Island west of the Shumagin Islands due to the similarity of the accretionary and intrusive surficial rocks (e.g., Bradley et al., 2003) (Figure 1c). However, crustal thickness becomes variable within and westward of the Shumagin Islands region, being reduced in places to about 30 km, and the lower crust has a higher velocity (~3.9 km s<sup>-1</sup>) beneath the Shumagin Islands. Thus the Shumagin islands may represent a major change in forearc morphology, defining a transition from thick accretionary crustal material and thicker forearc crust to the east to more conventional forearc crust to the west. Alternatively, the forearc crust in the Shumagin region may have been thinned and modified by deformation at the edge of the Beringian margin that led to the formation of a series of extensional basins in this region in the Oligocene-Miocene (e.g., Horowitz et al., 1989; Bécel et al., 2017; von Huene et al., 2019; Kahrizi et al., 2024).

The along-strike and down-dip variations in the thickness and velocity of the forearc crust above the megathrust could be important for the mechanical properties of the megathrust, with implications for strain accumulation and release (Sallarès & Ranero, 2019; Bassett et al., 2022). Although the recent 2020 M7.8 Simeonof and 2021 M8.2 Chgnik earthquakes occurred at similar depth ranges in the Shumagin and Semidi forearc regions (e.g., Liu et al., 2023), the differences in crustal thickness along strike suggest that rupture zone of the 2021 M8.2 earthquake in the Semidi segment is overlain by continental crust (orange star in Figure 7c), but that part of the rupture zone of the 2020 M7.8 in the Shumagin segment may have occurred below the continental Moho (Shillington et al., 2022) (Figure 5a; yellow star in Figure 7b); complexity of megathrust properties near the continental Moho are speculated to contribute to the patchiness of the M7.8 event (Shillington et al., 2022; Liu et al., 2023). In the Semidi segment, the recent rupture in the 2021 M8.2 event is confined to depths of ~26-42 km (Liu et al., 2023), the portion of the megathrust overlain by relatively high-velocity crust. The shallower megathrust overlain by low-velocity crust has recently been observed to host a slow slip event in 2018 and aseismic afterslip following the 2021 event (Brooks et al., 2023; He et al., 2023). These correlations suggest that the overriding plate could influence megathrust slip behavior. Downdip changes in bulk rigidity or permeability of the overriding plate and/or in frictional properties on the megathrust due to the overriding plate are proposed to influence megathrust behavior in other locations (Sallarès & Ranero, 2019; Bassett et al., 2022). Finally, differences in overriding plate structure and present-day inputs to the subduction zone could also influence megathrust frictional properties and heterogeneity. Low velocities in the outer forearc of the Semidi and Kodiak segments shown here could indicate significant underplating in the past (Moore et al., 1991), and thicker sedimentary sections are subducting in these segments today than farther west (e.g., von Huene et al., 2012; J. Li et al., 2018). Extensive sediment subduction is likely to reduce the inherent roughness of the plate interface and produce a large, smooth megathrust fault zone favorable to great earthquakes (Bangs et al., 2015; Scholl et al., 2015). Global studies suggest

higher seismic coupling and propensity for great earthquakes in regions with substantial sediment subduction and underplating (Ruff, 1989; Heuret et al., 2012).

5.2 Volcanic arc, mantle-wedge corner, and backarc structure

The mantle wedge structure is characterized by low shear velocities (4.1-4.3 km s<sup>-1</sup>) in the upper mantle beneath the volcanic arc. The Kodiak and Semidi segments have adequate resolutions in the backarc and both reveal continuous low-velocity anomalies sloping upward from more than 100 km depth beneath the backarc to the Moho beneath the volcanic front (Figure 7c-d). Similar inclined low-velocity zones have been observed at many volcanic arcs around the world, and are generally interpreted as the zone of hydrous partial melting and melt transport above the slab (e.g., Zhao et al., 2007; Wiens et al., 2008; Ward & Lin, 2018; Yang & Gao, 2020). These results suggest that a significant portion of the partial melt formation in the Alaska mantle wedge occurs beneath the backarc rather than immediately beneath the volcanic arc. Melt is transported along the inclined zone by porous and channelized flow to the Moho beneath the volcanoes (C. R. Wilson et al., 2014; Cerpa et al., 2018).

Unlike for some arcs, identified in the compilation of Abers et al. (2017), there is no indication of a high-velocity mantle wedge seaward of the volcanic arc. Instead, low mantle velocities extend seaward from the volcanic front into the corner of the mantle wedge (label 2 in Figure 7c-d). Partial melt does not provide a good explanation for these low velocities, since melt is highly buoyant and there is no magmatism observed on the forearc side of the volcanic front. In addition, heat flow anomalies characteristic of magma supply to the crust are limited to the volcanic arc and backarc regions in most arcs (Furukawa, 1993; Rees Jones et al., 2018). The low velocities in the wedge corner instead could result from serpentinization of the mantle peridotite by water released from the slab immediately below (Hyndman & Peacock, 2003; Reynard, 2013). The reduced shear velocities in the wedge corner of 4.1-4.3 km s<sup>-1</sup> are compatible with P-wave velocities of 7.3-8.0 km s<sup>-1</sup> from P-wave tomography in the Shumagin region (Abers, 1994).

The amount of forearc mantle serpentinization can be estimated from the velocity reduction along Lines 1, 2, and 3 (Figure 7b-d). The low velocity at the inner forearc uppermost mantle is  $4.29 \pm 0.08$  km s<sup>-1</sup> for Line 1,  $4.21 \pm 0.10$  km s<sup>-1</sup> for Line 2, and  $4.19 \pm 0.09$  km s<sup>-1</sup> for Line 3. Because the velocities are similar to one another within the uncertainty estimates, the inferred serpentinization is comparable for the three lines and we cannot infer along-strike variations. The experimental relationship between shear velocity V<sub>S</sub> and serpentine volume fraction ( $\Phi$ ) at 600 MPa is  $V_S = 4.51 - 2.19\Phi$  for lizardite and chrysotile, and  $V_S = 4.51 - 0.84\Phi$ for antigorite (Ji et al., 2013). Experimental work suggests that serpentinization of mantle peridotite forms mostly lizardite at temperatures below 500°C (e.g., Nakatani & Nakamura, 2016), as expected for the uppermost mantle with ages around 50 Ma (Stein & Stein, 1992; McKenzie et al., 2005). The assumption of lizardite mineralogy also results in a conservative estimate of the serpentinization percentage and water content of the mantle. Assuming an average value of the mantle wedge corner velocity of  $4.23 \pm 0.09$  km s<sup>-1</sup>, the corresponding mantle serpentinization above the slab in the wedge corner is roughly  $13 \pm 4$  vol%. Such a range of forearc mantle serpentinization is lower than the value of 20-35 vol% estimated by Yang and Gao (2020) along the Aleutian arc, where they observed a low velocity of 3.7-4.1 km s<sup>-1</sup> in the forearc mantle. Also this estimate of forearc mantle serpentinization is distinctly lower than a previous estimate by Bostock et al. (2002) for Cascadia, inferred from the velocity change across the crust-mantle boundary beneath the forearc. However, it is consistent with Abers et al (2017), who concluded that forearc mantle wedges show only modest degrees of serpentinization.

The backarc crust shows significant along-strike variations. In the northeast part of the study region, the backarc is characterized by a relatively typical continental crust with a thickness of about 35 km. However, in southern Bristol Bay, crust with significantly reduced thickness (~28 km) is found just to the north of the Alaska Peninsula and the active volcanic arc (Figure 5a). The entire region of Bristol Bay is underlain by a ~10 km thick layer of high velocity (~4.0 km s<sup>-1</sup>) lower crust (label 3 in Figure 7c) that we interpret as mafic underplating (Thybo and Artemieva, 2013). The ~4.0 km s<sup>-1</sup> shear velocity is consistent with the typical  $V_P$  observed for mafic underplating given that lower crustal mafic rocks have high  $V_P/V_S$  ratios (Thybo & Artemieva, 2013). The high-velocity lower crust indicates a dense mafic composition, resulting in a crust with a higher average density. Negative buoyancy caused by this denser crust as well as the reduced crustal thickeness result in lower elevations in Bristol Bay relative to backarc regions farther to the northeast.

Active-source surveys have shown a significant sedimentary sequence in the Bristol Bay Basin (Marlow et al., 1994; Walker et al., 2003). Bond et al. (1988) suggested that the basin formed primarily by flexural subsidence caused by the Oligocene to present crustal thickening of the Alaska Peninsula. In contrast, Walker et al. (2003) proposed that the basin was initially formed through tectonic extension. In the Walker et al. (2003) model, an early or middle Eocene through late Miocene phase of extension led to fault-controlled subsidence, then a late Eocene through Holocene phase of volcanic-arc loading or northward prograding delta led to flexural subsidence. Our observation of the thinner crust with a dense high-velocity mafic lower crust beneath the Bristol Bay basin supports Walker et al. (2003) model, with the dense lower crustal underplate emplaced during tectonic extension and associated magmatism.

### 5.3 Incoming plate hydration

The incoming plate structure clearly shows a low-velocity zone at the top of the subducting oceanic mantle (Figure 7). The velocities decrease towards the trench and show significant along-strike variations. Low-velocity zones at the top of the incoming plate mantle have been observed at many other subduction zones and are generally attributed to the serpentinization of mantle peridotite (Ivandic et al., 2008; Van Avendonk et al., 2011; Shillington et al., 2015; Cai et al., 2018; Mark et al., 2023) and/or to the effects of water in plate-bending faults (Miller & Lizarralde, 2016; Korenaga, 2017). The Shumagin segment shows a distinct low-velocity zone (~3.65 km s<sup>-1</sup>) at the top of the incoming plate mantle, suggesting strong hydration if the velocity reduction is due to serpentinization. In contrast, the Semidi segment and Kodiak segment show much weaker hydration of the incoming Pacific plate, with a velocity reduction only to ~4.05 km s<sup>-1</sup> and ~4.0 km s<sup>-1</sup>, respectively.

The extent of incoming plate hydration can be better compared using velocity profiles at locations near the trench axis (Figure 8). Since the resolution of the incoming plate in the Kodiak segment (Line 3; Figure 7d) is limited by the small number of nearby OBSs returning data (Figure 2), we only make the comparison between the Shumagin segment (Line 3; Figure 7b) and the Semidi segment (Line 3; Figure 7c). We choose the trench profiles of both Shumagin and Semidi segments at locations 20 km seaward from the trench axis to limit the smoothing effect of surface waves. To evaluate the magnitude of mantle hydration, we also need a reference profile

that represents an unaltered oceanic plate structure. The seaward end points of those projection lines are the possible candidates. The resolution at the seaward end of Line 2 is the best among all segments and at a significant distance away from the trench axis, thus we choose the seaward end of Line 2 to be a reference profile giving the velocity structure of the unaltered incoming plate in the region (Figure 8a). By comparing the shear velocity profiles, we observe that the magnitude of velocity reduction and thus incoming plate hydration is stronger in the Shumagin segment than that in the Semidi segment, consistent with the active source results from Shillington et al (2015). Although the reference velocity profile also shows a small velocity reduction (~0.1 km s<sup>-1</sup>) atop the mantle, tests in which a series of synthetic dispersion curves were inverted using the same parameterization suggest that the magnitude of such a small velocity reduction was not well constrained by the dispersion data. Besides, we note that the active source profile in this region also shows a significant increase in P-wave velocity with depth beneath the moho farther from the trench, consistent with the reference profile.

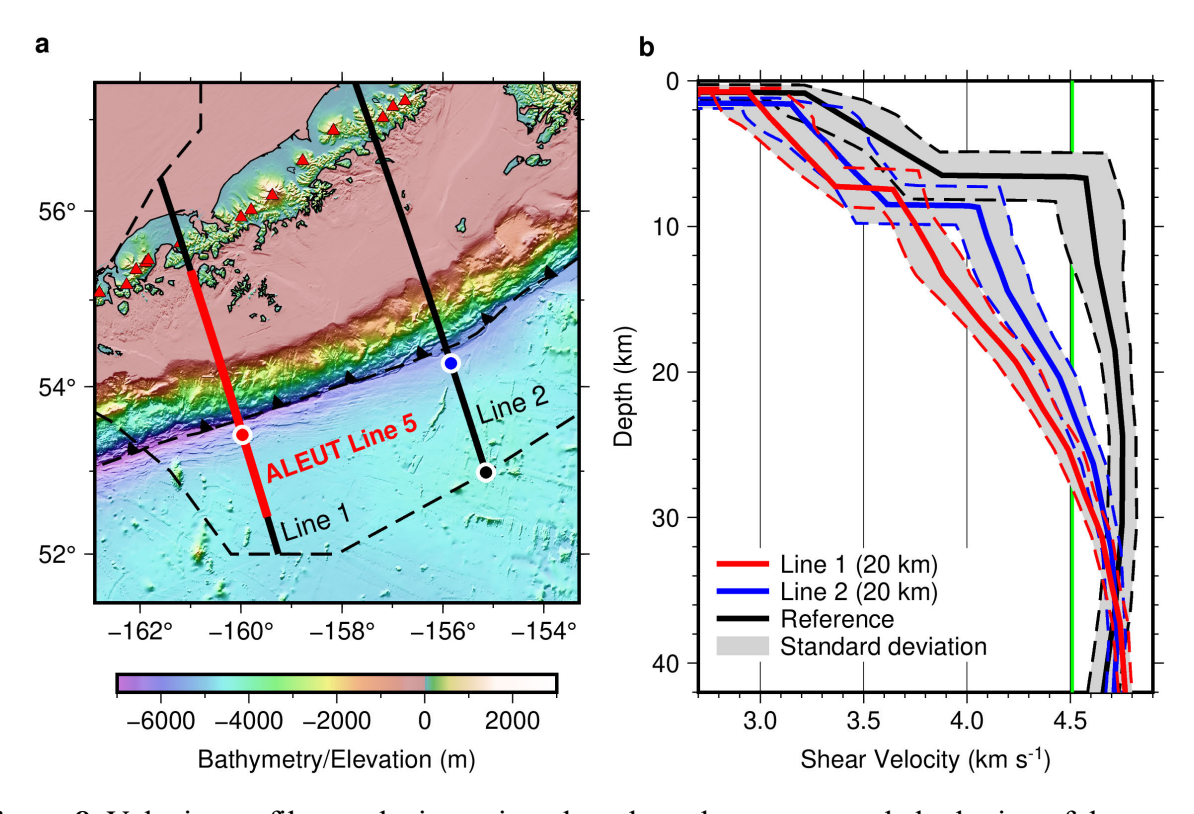


**Figure 8**. Velocity profiles on the incoming plate show the upper mantle hydration of the Shumagin segment and the Semidi segment. (a) The locations of velocity profiles on cross sections. The red circle on Line 1 and blue circle on Line 2 are chosen 20 km seaward away from the trench axis so that they represent the hydration status at the trench and minimize the spatial smoothing of surface waves. The black circle at the seaward end of Line 2 gives the location of the velocity profile representing the unaltered oceanic plate structure. ALEUT Line 5, shown as the red line, is part of Line 1 (Shillington et al., 2022). (b) The 1-D shear velocity profiles of the reference, Line 1 near the trench, and Line 2 near the trench. Here the profile near the trench is chosen at 20 km seaward from the trench axis. The uncertainty contours of each are shown as

gray zones. The experimental velocity value of unaltered upper mantle peridotite, 4.51 km s<sup>-1</sup>, is marked as a green line. The depth is relative to the seafloor.

Assuming the velocity reduction atop the mantle is purely due to serpentinization, we could use the shear velocity reduction to constrain the hydration. We still follow the method described in Section 5.2 to estimate the serpentinization (McKenzie et al., 2005; Ji et al., 2013; Nakatani & Nakamura, 2016). Although the reference velocity profile shows uppermost mantle velocities ranging from 4.55 km s<sup>-1</sup> to 4.7 km s<sup>-1</sup>, here we use the experimental value of 4.51 km s<sup>-1</sup> as the reference velocity of unaltered upper mantle peridotite, which provides a further conservative estimate of the degree of serpentinization and facilitates comparison with other studies. In the Shumagin segment, the shear velocity reduction is  $0.87 \pm 0.12$  km s<sup>-1</sup> immediately below the Moho (Figure 8b). The velocity reduction then becomes smaller with depth until there is no velocity reduction at  $18 \pm 3$  km below the Moho. The corresponding hydration is roughly equivalent to a  $40 \pm 6$  vol% serpentinization at the top of the mantle, reducing to no serpentinization at  $18 \pm 3$  km below the Moho.

Similar calculations can be made for the Semidi segment. Using 4.51 km s<sup>-1</sup> as the reference value, a  $0.46\pm0.13$  km s<sup>-1</sup> shear velocity reduction is observed right below the Moho, decreasing to no velocity reduction at  $14\pm3$  km below the Moho. This gives an estimate of  $21\pm6$  vol% serpentinization at the top of the mantle, decreasing to zero at  $14\pm3$  km below the Moho.

The maximum degree of serpentinization, as well as the total thickness of the serpentinized layer, is larger in the Shumagin segment compared to that in the Semidi segment, consistent with previous active source results (Shillington et al., 2015). Using the shear velocity reduction at the uppermost mantle, we find that the serpentinization in the Shumagin segment is approximately two times greater than that in the Semidi segment. Carried by the hydrous minerals, more water is expected to input into the deep Earth through the Shumagin segment in the Alaska subduction zone.

The distribution of mantle velocity reduction is similar to the distribution of seismicity located by AACSE ocean bottom seismographs (Matulka & Wiens, 2022) as well as mapped fault scarps in seafloor bathymetry (Clarke, 2022) and seismic reflection images (Shillington et al., 2015), consistent with the idea that velocity reduction is caused by hydration from plate-bending faults penetrating into the upper mantle. A recent magnetotelluric study along the Shumagin segment suggests a source of fluids at depth of 15-25 km beneath the Moho in the forearc that they interpreted as due to dehydration of serpentinized mantle (Cordell et al., 2023). The Shumagin section shows numerous plate bending faults and has a high seismicity rate, compared to the near-absence of seafloor faults and a lower seismicity rate in the Semedi segment. The depth extent of inferred serpentinization along the Shumagin segment coincides with the depth range of normal faulting earthquakes along plate bending faults (Matulka & Wiens, 2022). The maximum incoming plate seismicity rate occurs 5-10 km below the Moho, and earthquakes are largely limited to depths less than 15-20 km below the Moho, coinciding with the lower limit of serpentinization from this study. The depth range of seismicity in the Semidi segment is similar, but with a much lower seismicity rate.

It is worthwhile to compare the Alaska Trench results with the central Mariana Trench (Cai et al., 2018) and the southern Mariana Trench (Zhu et al., 2021). Since the studies use

similar techniques, we can directly compare the V<sub>S</sub> profiles. The near-trench regions of the central Mariana Trench show uppermost mantle  $V_S$  reduced to ~3.5 km s<sup>-1</sup>, lower than the ~3.65 km s<sup>-1</sup> observed in the Shumagin segment. In addition, the lowered seismic velocities in Mariana extend to about 24 km below the Moho, compared to only 18 km below the Moho in the Shumagin segment. Similar, but less well-constrained velocities and depths were found by Zhu et al. (2021) in the southern Mariana Trench. Cai et al. (2018) interpreted the extremely low incoming plate mantle velocities at the trench as partly due to pore water in the bending faults, and used a velocity of 4.1 km s<sup>-1</sup> found beneath the forearc after pore water would have been expelled for calculating the degree of serpentinization. The lower velocities and greater depth extent of the mantle velocity reduction suggest a larger percent and extent of mantle serpentinization for Mariana than in the Shumagin or Semidi segments of the Alaska Subduction Zone. The difference in the hydration of the incoming Alaska and Mariana plates is largely due to the differences in their oceanic plate age (Alaska ~50-55 Ma; Mariana ~150 Ma). The thicker, colder lithosphere at the Mariana Trench results in a deeper neutral plane and greater extensional strain above the neutral plane. Another factor is the distribution of outer rise plate-bending faults (abundant in the Mariana and the Shumagin segment of Alaska; fewer in the Semidi segment of Alaska). Finally, the overall geological setting of the Mariana subduction zone is more extensional, further enhancing shallow extensional faulting and deepening the neutral plane (Emry et al., 2014; Eimer et al., 2020).

844

845

846 847

848

849

850

851

852

853

854

855

856

857

858

859

860

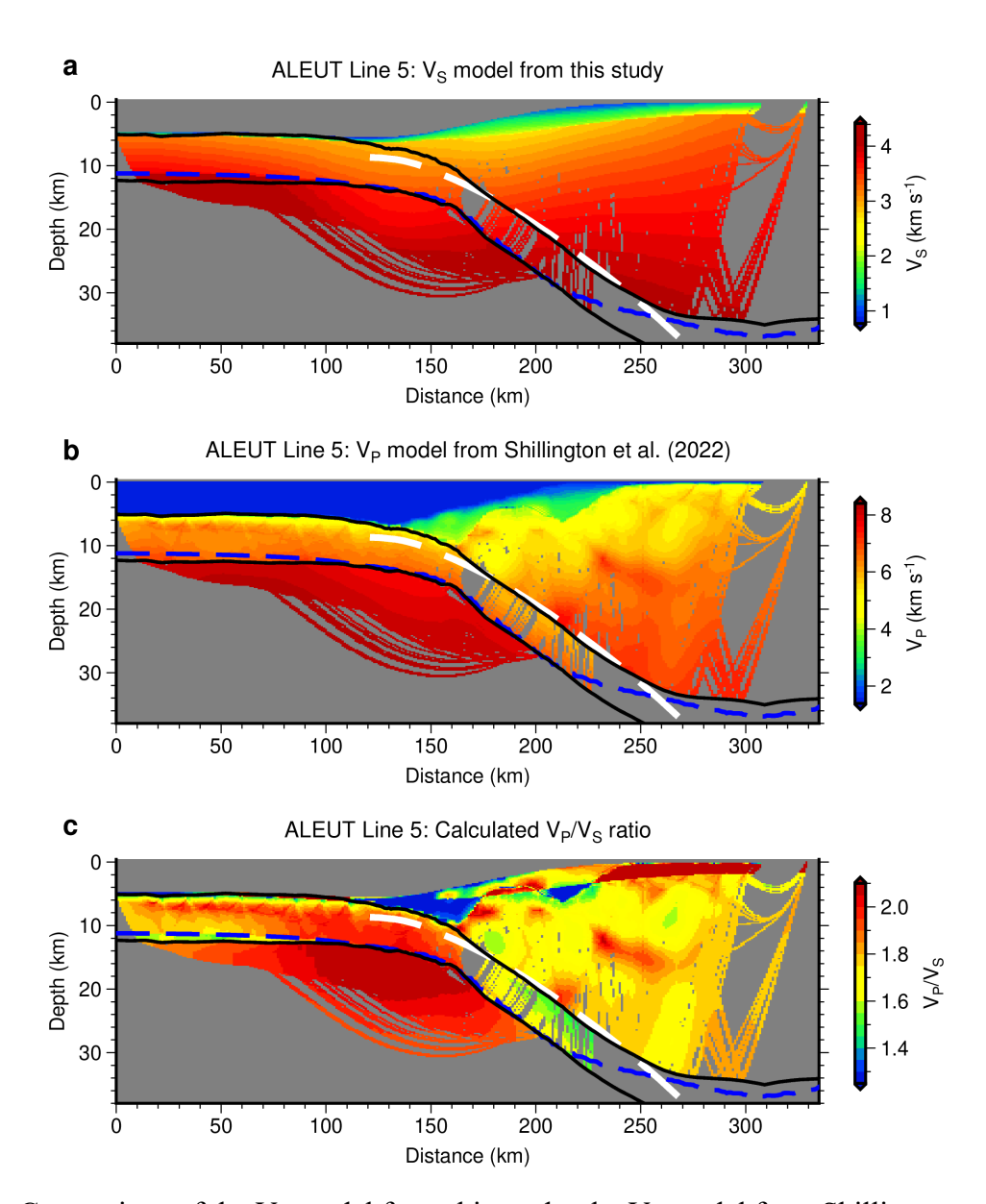


**Figure 9**. Comparison of the  $V_S$  model from this study, the  $V_P$  model from Shillington et al. (2022), and the calculated  $V_P/V_S$  ratio using two models. The white dashed line shows the depth of slab interface in the Slab2.0 model (Hayes et al., 2018). The two solid black lines show boundaries of the  $V_P$  model that are constrained by reflections (Shillington et al., 2022), which mark either the ocean bottom, the interface between the subducting plate and the overriding plate, Moho depth of the overriding plate, or Moho depth of the subducting plate. The dashed blue line shows the Moho depth of the  $V_S$  model constrained by this study. (a) The shear velocity ( $V_S$ ) model from this study, which is just a cross-section of the 3-D shear velocity model along the ALEUT Line 5. (b) The P-wave velocity ( $V_P$ ) model from Shillington et al. (2022), which is a 2-D model of the ALEUT Line 5 determined by joint refraction and reflection 2-D tomographic inversion. (c) The calculated  $V_P/V_S$  ratio using two models along ALEUT Line 5. The colorbar is limited to show the 5- to 95-percentile range of all  $V_P/V_S$  values.

### 5.4 Comparison with previous active source results

The incoming plate hydration has been previously examined using active-source data (Shillington et al., 2015). In the Shumagin segment, the P-wave velocity of the upper mantle is reduced from 8.2 km s<sup>-1</sup> to 7.5 km s<sup>-1</sup>. In the Semidi segment, the P-wave velocities range between 8.0 km s<sup>-1</sup> to 7.7 km s<sup>-1</sup>, but do not show a systematic trenchward decrease; these variations may result from heterogeneity in intermediate spreading crust (Shillington et al., 2015). The experimental relationship between  $V_P$  and serpentine volume fraction ( $\Phi$ ) at 600 MPa is  $V_P = 8.10 - 3.00\Phi$  for lizardite and chrysotile (Ji et al., 2013). For the Shumagin segment, the lowest Vs of 3.64 km s<sup>-1</sup> is equivalent to ~40 vol% serpentinization, whereas the lowest  $V_P = 7.5$  km s<sup>-1</sup> is equivalent to ~20 vol% serpentinization. Clearly, the serpentinization immediately beneath the Moho estimated from shear velocity reduction tends to be higher than estimates from P-wave velocities.

To investigate the differences in hydration estimated from  $V_P$  and  $V_S$ , we compare the shear velocity model with the active-source P-wave model along the ALEUT Line 5 (Shillington et al., 2022) (Figure 9). The  $V_P$  and  $V_S$  structures along the same projection line show similar features, though the active source P-wave model exhibits more details and the shear velocity model shows the smoothing effect of surface waves (Figure 9a; Figure 9b). The  $V_P/V_S$  ratio (Figure 9c) calculated from the two models shows some small features with extreme values due to the higher resolution and different settings of the slab in the active source P-wave model, but are in general consistent with expected ratios for oceanic and forearc crust. For example, most of the forearc crust has  $V_P/V_S$  ratios between 1.65 and 1.85, which is typical for the continental crust (N. I. Christensen, 1996).

The crust of the incoming plate shows a distinct region of high  $V_P/V_S$  ratio in the plate bending region near the trench. Previous active source studies show large  $V_S$  reductions and  $V_P/V_S$  ratio increases in the crust of plate-bending regions of various subduction zones (Fujie et al., 2013; Fujie et al., 2018; Grevemeyer et al., 2018). This is generally interpreted as due to the hydration of crustal rocks as well as the additional effect of water in joints and cracks. The high  $V_P/V_S$  ratio of the crust of the incoming plate is generally greater than 1.9 for both Kuril Trench and Japan Trench (Fujie et al., 2018), also quite similar to what we observe here (Figure 9c).

The incoming plate mantle shows an extremely high  $V_P/V_S$  ratio of greater than 2.05 near the trench axis. The experimental relationship between  $V_P/V_S$  ratio and serpentine volume fraction ( $\Phi$ ) at 600 MPa is  $V_P/V_S = 1.77 + 0.38\Phi$  for lizardite and chrysotile, and  $V_P/V_S = 1.77 + 0.04\Phi$  for antigorite (Ji et al., 2013). Using the  $V_P/V_S = 1.77 + 0.38\Phi$  relationship and  $V_P/V_S = 2.05$ , we can estimate the serpentinization from  $V_P/V_S$  for the uppermost mantle in the Shumagin segment as 73 vol%. This value, of course, is unrealistic but suggests that the serpentinization implied by the  $V_S$  reduction,  $V_P$  reduction, and  $V_P/V_S$  increase are inconsistent.

The discrepancy between estimates of serpentinization from  $V_P$ ,  $V_S$ , and the  $V_P/V_S$  ratio may result from the effect of water in joints and cracks. Poroelastic calculations by Takei (2002) show that for water-filled cracks with large aspect ratios, as expected in partially serpentinized peridotite, the fractional velocity reduction in  $V_S$  is significantly larger than the fractional reduction in  $V_P$ . Korenaga et al. (2017) also showed that modest porosity in crack-like pore spaces with large aspect ratios lowers  $V_S$  more significantly than  $V_P$  and increases the  $V_P/V_S$  ratio. Cai et al. (2018) attributed part of the large  $V_S$  reduction in the Mariana outer-rise mantle to water in cracks and joints. Mark et al. (2023) found evidence from seismic anisotropy for

water in crack-like pores in the upper 1 km of the Mariana outer rise mantle using active-source data. If the water in crack-like porosity exists in the mantle, the percent serpentinization determined by  $V_S$  values and the  $V_P/V_S$  ratios will be overestimated.

In the following discussion, we assume that the percent serpentinization of the mantle immediately below the Moho is better estimated by the V<sub>P</sub> reduction determined by active source data (Shillington et al., 2015), since we observe that the water porosity has a more limited influence on V<sub>P</sub>. However, the maximum depth of serpentinization is determined by this study due to the limited depth penetration of the active source results. This discussion assumes that percent serpentinization can be estimated using formulas for bulk serpentinization, as has traditionally been done in previous studies (e.g., Grevemeyer et al., 2018). The actual situation may be more complex, as the serpentinization may be localized in narrow regions surrounding discrete faults (Hatakeyama et al., 2017). In this case, there will be frequency-dependent wave propagation through the mantle at the frequencies used in active source studies (Miller & Lizarralde, 2016; Miller et al., 2021; Mark et al., 2023). Estimates of serpentinization taking this effect into account generally result in smaller percentages of serpentinization, but require analysis of azimuthal anisotropy, which is not available in this case. Therefore we will use the serpentinization estimates based on bulk serpentinization given by Shillington et al. (2015).

#### 5.5 Quantitative estimates of subducted water

The amount of bound water carried into the Alaska subduction zone by the subducting mantle can be assessed, given estimates of the percentage serpentinization as a function of depth on the incoming plate, since both lizardite and antigorite contain 13% water by weight. The water content of the mantle by weight is calculated from

$$w_h = w_s \alpha_s \rho_s / \rho_m \tag{2}$$

where  $w_s$  is the weight fraction of water in serpentine,  $\alpha_s$  is the volume fraction of serpentine in the mantle determined from seismic measurements, and  $\rho_s$  and  $\rho_m$  are the densities of serpentine and the mantle, respectively (Carlson & Miller, 2003). Here we assume that serpentinization is maximum at the Moho, where the percent serpentinization is determined from the  $V_P$  velocity reduction, and decreases linearly to the maximum depth of serpentinization determined from this study. We do not include any liquid water in pore spaces, since this water will be eliminated with increasing pressure (David et al., 1994) and will not be subducted to significant depths. We also do not explicitly include possible hydrous minerals other than serpentine, such as chlorite and brucite, but note that these other hydrous minerals will also lower the seismic velocity in a similar way to serpentine. Experimental evidence indicates that the dominant hydrous mineral in the incoming plate mantle is likely to be lizardite serpentine (Okamoto et al., 2011).

For the Shumagin segment, the V<sub>P</sub> reduction from Shillington et al (2015) gives 20 vol% serpentinization at the Moho, decreasing to zero at 18 km below the Moho. The total water content of the hydrated mantle at the Shumagin segment is then equivalent to an 18 km thick, partially serpentinized (10 vol% serpentine, thus 1.0 wt% water) slab mantle layer. Applying the convergence rate of 66 mm yr<sup>-1</sup> (DeMets et al., 2010), the amount of mantle water input into the Shumagin segment is 37 Tg Myr<sup>-1</sup> m<sup>-1</sup>.

A similar calculation for the Semedi segment is more uncertain because the evidence of  $V_P$  reduction from hydration is less clear in the active-source data.  $V_P$  is apparently reduced to 7.7 km s<sup>-1</sup>, but it is unclear whether this is due to hydration or to variability associated with

intermediate spreading crust. The  $V_S$  reduction observed in this study suggests the reduction is likely due to hydration, in which case we can calculate a serpentinization of 13 vol% from the  $V_P$  reduction using the relationships in Ji et al. (2013). Assuming that the serpentinization decreases linearly from 13 vol% at the Moho to zero at a depth of 14 km below the Moho, this is equivalent to a 14 km thick, partially serpentinized (6.5 vol% serpentine, thus 0.6 wt% water) hydrated mantle layer. With the convergence rate of 63 mm yr $^{-1}$  (DeMets et al., 2010), this provides an estimate of 17 Tg Myr $^{-1}$  m $^{-1}$  for the flux of mantle water into the Semidi segment. This indicates that the subducting mantle carries more than twice as much water into the Shumagin segment compared to the Semidi segment.

These estimates necessarily involve a number of assumptions and are thus only very approximate, but are improvements on previous estimates that made ad-hoc assumptions about the hydration of the subducting mantle (e.g., van Keken et al., 2011), which had no constraint on the depth extent of the serpentinized layer. The largest uncertainty in these estimates is associated with the volume percent of serpentinization, due to the uncertainty of interpreting the discrepant estimates from  $V_P$ ,  $V_S$ , and  $V_P/V_S$ , as well as the possible effects of liquid water in crack-like porosity (Korenaga et al., 2017) and anisotropy (Miller & Lizarralde, 2016; Mark et al., 2023). All of the assumptions made in our estimations are conservative and thus result in a minimum estimate of subducting water in each segment.

These new estimates of subducted mantle water can be combined with previous estimates of water subducted in the crust and sediments to estimate the total water flux. van Keken et al. (2011) did not divide the segments, but estimated that 18 Tg Myr<sup>-1</sup> m<sup>-1</sup> subducts in the crust and sediments into the Alaska subduction zone offshore the Alaska Peninsula. Adding this to the mantle estimates gives total subducted water estimates of 55 Tg Myr<sup>-1</sup> m<sup>-1</sup> for the Shumagin segment and 35 Tg Myr<sup>-1</sup> m<sup>-1</sup> for the Semidi segment. Because the degree of mantle hydration was nearly unconstrained, van Keken et al. (2011) calculated three scenarios for mantle hydration. These estimates were 18 Tg Myr<sup>-1</sup> m<sup>-1</sup> for no hydration, 26 Tg Myr<sup>-1</sup> m<sup>-1</sup> for 2 wt% water in a 2 km thick mantle layer beneath the Moho, and 53 Tg Myr<sup>-1</sup> m<sup>-1</sup> for full serpentinization of a 2 km thick layer. The new estimates exceed the intermediate scenario for both the Shumagin and Semidi segments, and the new estimate for Shumagin is almost identical to the full serpentinization scenario of van Keken et al. (2011).

The water flux estimates for both Shumagin and Semidi segments are much less than the 94 Tg Myr<sup>-1</sup> m<sup>-1</sup> estimated for the total water flux at the Mariana Trench (Cai et al., 2018). This difference results partly from the greater inferred percent serpentinization and the greater depth extent of serpentinization for Mariana. The greater depth extent, as indicated by both the velocity structure and the greater depth of plate bending earthquakes for the Mariana incoming plate (Eimer et al., 2020), may result at least in part from the greater age, and thus greater thickness, of the Mariana lithosphere. An older plate has a colder thermal condition and the serpentine could be stable to a greater depth. Antigorite is the main stable phase of serpentine at high temperatures, up to ~630°C at 1 GPa (Reynard, 2013; Schwartz et al., 2013). From the recent plate cooling model (Richards et al., 2018), the thermal condition limit of 600°C is 25 km below the seafloor for a 50 Ma plate, and 45 km below the seafloor for a 150 Ma plate. Moreover, the neutral plane is deeper for older lithosphere and produces a mechanism that could cause deeper stable depth (e.g., Sandiford & Craig, 2023). In addition, the overall extensional stress field of the Mariana arc may be a contributing factor; the slab in the Marianas is dipping more steeply than in the Alaska subduction zone (Nishikawa & Ide, 2015; Hayes et al., 2018).

Comparisons of the mantle water flux estimates for Shumagin and Semidi segments and the central Mariana subduction zone suggest that hydration of the uppermost mantle at subduction zones is highly variable, not only for different subduction zones, but also for different segments of the same subduction zone. In Section 5.3, we have discussed the strong correlation between the distribution of mantle hydration, seismicity, and outer rise faults (Clarke, 2022; Matulka & Wiens, 2022), and that the depth extent of mantle hydration coincides with the depth range of normal faulting earthquakes along plate bending faults (Matulka & Wiens, 2022). The along-strike variation of mantle hydration in Alaska and Mariana is highly correlated with seismicity and earthquake ruptures, where strong mantle hydration leads to an abundance of small earthquakes and the absence of large megathrust earthquakes. Thus, along-strike changes in hydration can have major effects on intermediate depth and shallow thrust zone seismicity (Shillington et al., 2015; Wei et al., 2021; F. Wang et al., 2022).

#### **6 Conclusions**

We determine a 3-D isotropic shear velocity model of the Alaska subduction zone from a Bayesian Monte Carlo inversion of Rayleigh wave dispersion data using OBS and land station data acquired by the AACSE project and other nearby land networks. A joint inversion including P-wave receiver functions is carried out for land seismic stations.

The 3-D model shows major along-strike changes in structure. The forearc structure, including Kodiak Island, appears to have a relatively thick crust (35-42 km) and reduced lower crustal velocities (~3.5 km s<sup>-1</sup>) from the Kodiak segment to the eastern edge of the Shumagin segment. The eastern portion with distinctive thickened crust is just inboard of the slow lower crustal material extended from the Chugach Terrane. The crustal thickness becomes variable westward of the Shumagin Islands, suggesting that the Shumagin Islands may represent a major change in forearc morphology. The continuous low-velocity anomalies observed in the mantle wedge likely represent the hydrous partial melting and melt transport above the slab. The low mantle velocities that extend seaward of the volcanic front into the mantle wedge corner, however, are likely due to approximately 13 vol% serpentinization of the mantle peridotite by water released from the slab immediately below. As for backarc structure, most regions in the northeast are characterized by a relatively typical continental crust. The Bristol Bay Basin, however, shows a significantly reduced crustal thickness and a high-velocity lower crust, indicating a dense mafic composition emplaced during the tectonic extension process that formed the basin.

The incoming plate structure shows a low-velocity zone at the top of the subducting oceanic mantle, which results from the serpentinization of mantle peridotite due to water penetrating into the mantle through outer-rise plate-bending faults. Velocity reduction is greater and the thickness of the low-velocity region is larger in the Shumagin segment compared to the Semidi segment. Estimates of serpentinization percentage from  $V_S$  reductions and  $V_P/V_S$  ratios are larger than that estimated from  $V_P$  reduction in Shillington et al. (2015), suggesting that  $V_S$  may be strongly affected by liquid water in crack-like pores. Therefore we estimate the serpentinization percentage from the previous  $V_P$  results, but use the  $V_S$  results to constrain the thickness of the hydrated region. The amount of mantle water input into the strongly hydrated Shumagin segment is about 37 Tg Myr<sup>-1</sup> m<sup>-1</sup>, while the amount of mantle water input into the

1053 1054 1055 1056 1057 1058	Semidi segment is about 17 Tg Myr <sup>-1</sup> m <sup>-1</sup> . Thus the amount of mantle water input into the Shumagin segment is more than twice the mantle water flux into the Semidi segment. However, the amount of water input in both sections is much less than previously estimated for the Mariana incoming plate using similar methods. Water input into subduction zones bound as hydrous minerals in the mantle is highly variable, both between different subduction zones as well as between different segments of the same subduction zone.
1059	
1060	
1061	Acknowledgments
1062 1063 1064 1065 1066 1067 1068 1069 1070 1071 1072 1073 1074 1075	We thank all the field teams who collected the AACSE data, particularly the other PIs Geoffrey Abers, Aubreya Adams, Emily Roland, Susan Schwartz, Anne Sheehan, Spahr Webb, and Lindsay Worthington. We also thank the ship captains and crew, as well as the OBS engineers from Woods Hole and Lamont-Doherty. This work is supported by the National Science Foundation under grants OCE-2025969 and OCE-2026676 as well as a subcontract to Washington University from Cornell University. Seismic instruments and field support were provided by the EarthScope Consortium through the PASSCAL Instrument Center at New Mexico Tech. We also thank James Gaherty, Patrick Matulka and Jacob Clarke for helpful conversations.  The facilities of the EarthScope Consortium were used for access to waveforms and related metadata used in this study. These services are funded through the Seismological Facility for the Advancement of Geoscience (SAGE) Award of the National Science Foundation under Cooperative Support Agreement EAR-1851048.
1076	Open Research
1077 1078 1079 1080 1081 1082 1083 1084 1085 1086 1087 1088 1089	All seismic data were downloaded through the EarthScope Consortium Web Services (https://service.iris.edu/), including the following seismic networks: (1) XO (2018-2019) (AACSE) (Abers et al., 2018); (2) TA (USArray Transportable Array) (IRIS Transportable Array, 2003); (3) AK (Alaska Earthquake Center, 1987); (4) II (GSN – IRIS/IDA) (Scripps Institution of Oceanography, 1986); (5) AT (NTWC Alaska) (NOAA, 1967); (6) GM (U. S. Geological Survey, 2016); (7) YG (2016-2018) (WVLF) (D. H. Christensen & Abers, 2016); (8) AV (Alaska Volcano Observatory, 1988). The ambient noise processing code, FTAN analysis code, and ray-theoretic tomography code are from CU-Boulder Research Products ( <a href="http://ciei.colorado.edu/Products/">http://ciei.colorado.edu/Products/</a> ). The ASWMS package is from IRIS DMC Data Services Products ( <a href="https://ciei.colorado.edu/Products/aswms/">https://ciei.colorado.edu/Products/aswms/</a> ). We also used open-source software including ObsPy (Beyreuther et al., 2010) and GMT (Wessel et al., 2019) for data analysis and visualization.
1091	References
·	

- Abers, G. A. (1994). Three-dimensional inversion of regional P and S arrival times in the East Aleutians and sources of subduction zone gravity highs. *Journal of Geophysical Research: Solid Earth*, 99(B3), 4395-4412. doi:https://doi.org/10.1029/93JB03107
- Abers, G. A., van Keken, P. E., & Hacker, B. R. (2017). The cold and relatively dry nature of mantle forearcs in subduction zones. *Nature Geoscience*, 10(5), 333-337. doi:10.1038/ngeo2922
- Abers, G. A., Wiens, D., Schwartz, S., Sheehan, A., Shillington, D., Worthington, L., . . . Adams,

  A. (2018). AACSE: Alaska Amphibious Community seismic Experiment. Retrieved from:

  https://www.fdsn.org/networks/detail/XO\_2018/
- Acquisto, T. M., Bécel, A., & Canales, J. P. (2022a). 3D traveltime tomography of the Alaska subduction zone through inversion of active source data acquired during the Alaska Amphibious Community Seismic Experiment (AACSE). Paper presented at the AGU Fall Meeting, Chicago, IL. <a href="https://ui.adsabs.harvard.edu/abs/2022AGUFM.T25E0169A">https://ui.adsabs.harvard.edu/abs/2022AGUFM.T25E0169A</a>
- Acquisto, T. M., Bécel, A., Singh, S. C., & Carton, H. (2022b). Evidence of Strong Upper
  Oceanic Crustal Hydration Outboard the Alaskan and Sumatran Subduction Zones.

  Journal of Geophysical Research: Solid Earth, 127(10), e2022JB024751.

  doi:https://doi.org/10.1029/2022JB024751
- Alaska Earthquake Center, Univ of Alaska Fairbanks. (1987). *Alaska Geophysical Network*.

  Retrieved from: <a href="https://www.fdsn.org/networks/detail/AK/">https://www.fdsn.org/networks/detail/AK/</a>
- Alaska Volcano Observatory, USGS. (1988). *Alaska Volcano Observatory*. Retrieved from: <a href="https://www.fdsn.org/networks/detail/AV/">https://www.fdsn.org/networks/detail/AV/</a>
- Arnulf, A. F., Bassett, D., Harding, A. J., Kodaira, S., Nakanishi, A., & Moore, G. (2022).

  Upper-plate controls on subduction zone geometry, hydration and earthquake behaviour.

  Nature Geoscience, 15(2), 143-148. doi:10.1038/s41561-021-00879-x
- Aziz Zanjani, F., & Lin, G. (2022). Double Seismic Zones along the Eastern Aleutian-Alaska Subduction Zone Revealed by a High-Precision Earthquake Relocation Catalog. Seismological Research Letters, 93(5), 2753-2769. doi:10.1785/0220210348
- Bangs, N. L., McIntosh, K. D., Silver, E. A., Kluesner, J. W., & Ranero, C. R. (2015). Fluid accumulation along the Costa Rica subduction thrust and development of the seismogenic zone. *Journal of Geophysical Research: Solid Earth, 120*(1), 67-86. doi:10.1002/2014JB011265
- Barcheck, G., Abers, G. A., Adams, A. N., Bécel, A., Collins, J., Gaherty, J. B., . . .

  Worthington, L. L. (2020). The Alaska Amphibious Community Seismic Experiment.

  Seismological Research Letters. doi:10.1785/0220200189
- Barmin, M. P., Ritzwoller, M. H., & Levshin, A. L. (2001). A Fast and Reliable Method for Surface Wave Tomography. *pure and applied geophysics*, *158*(8), 1351-1375. doi:10.1007/PL00001225
- Bassett, D., Arnulf, A., Henrys, S., Barker, D., van Avendonk, H., Bangs, N., . . . Yamamoto, Y. (2022). Crustal Structure of the Hikurangi Margin From SHIRE Seismic Data and the Relationship Between Forearc Structure and Shallow Megathrust Slip Behavior. *Geophysical Research Letters*, 49(2), e2021GL096960.
- doi:https://doi.org/10.1029/2021GL096960
- Bécel, A., Shillington, D. J., Delescluse, M., Nedimović, M. R., Abers, Geoffrey A., Saffer, D.
- M., . . . Kuehn, H. (2017). Tsunamigenic structures in a creeping section of the Alaska subduction zone. *Nature Geoscience*, 10(8), 609-613. doi:10.1038/ngeo2990

- Bell, S. W., Forsyth, D. W., & Ruan, Y. (2014). Removing Noise from the Vertical Component Records of Ocean-Bottom Seismometers: Results from Year One of the Cascadia Initiative. *Bulletin of the Seismological Society of America*, 105(1), 300-313. doi:10.1785/0120140054
- Bensen, G. D., Ritzwoller, M. H., Barmin, M. P., Levshin, A. L., Lin, F., Moschetti, M. P., . . . Yang, Y. (2007). Processing seismic ambient noise data to obtain reliable broad-band surface wave dispersion measurements. *Geophysical Journal International*, 169(3), 1239-1260. doi:10.1111/j.1365-246X.2007.03374.x
- Berg, E. M., Lin, F.-C., Allam, A., Schulte-Pelkum, V., Ward, K. M., & Shen, W. (2020). Shear Velocity Model of Alaska Via Joint Inversion of Rayleigh Wave Ellipticity, Phase Velocities, and Receiver Functions Across the Alaska Transportable Array. *Journal of Geophysical Research: Solid Earth*, 125(2), e2019JB018582. doi:10.1029/2019JB018582
- Beyreuther, M., Barsch, R., Krischer, L., Megies, T., Behr, Y., & Wassermann, J. (2010). ObsPy:

  A Python Toolbox for Seismology. *Seismological Research Letters*, 81(3), 530-533.

  doi:10.1785/gssrl.81.3.530
- Bond, G. C., Lewis, S. D., Taber, J., Steckler, M. S., & Kominz, M. A. (1988). Evidence for formation of a flexural backarc basin by compression and crustal thickening in the central Alaska Peninsula. *Geology*, 16(12), 1147-1150. doi:10.1130/0091-7613(1988)016<1147:EFFOAF>2.3.CO;2
- Bostock, M. G., Hyndman, R. D., Rondenay, S., & Peacock, S. M. (2002). An inverted continental Moho and serpentinization of the forearc mantle. *Nature*, 417(6888), 536-538. doi:10.1038/417536a
- Bradley, D. C., Kusky, T. M., Haeussler, P. J., Goldfarb, R. J., Miller, M. L., Dumoulin, J. A., . .

  1160

  Karl, S. M. (2003). Geologic signature of early Tertiary ridge subduction in Alaska. In

  V. B. Sisson, S. M. Roeske, & T. L. Pavlis (Eds.), Geology of a transpressional orogen

  1162

  developed during ridge-trench interaction along the North Pacific margin (Vol. 371, pp.

  0): Geological Society of America.
- Brooks, B. A., Goldberg, D., DeSanto, J., Ericksen, T. L., Webb, S. C., Nooner, S. L., . . . Nevitt, J. (2023). Rapid shallow megathrust afterslip from the 2021 M8.2 Chignik, Alaska earthquake revealed by seafloor geodesy. *Sci Adv*, *9*(17), eadf9299. doi:10.1126/sciadv.adf9299
- Bruns, T. R., von Huene, R. E., Culotta, R. C., & Lewis, S. D. (1985). Summary geologic report for the Shumagin outer continental shelf (OCS) planning area, Alaska (85-32). Retrieved from http://pubs.er.usgs.gov/publication/ofr8532
- Burstein, J. A., Shillington, D. J., Becel, A., & Nedimovic, M. R. (2022). Crustal Structure of the
  Semidi Segment in the Alaska Subduction Zone Across the 2021 Mw8.2 Chignik
  Earthquake Rupture Area Revealed from 2D Wide-Angle Reflection/Refraction Seismic
  Data. Paper presented at the AGU Fall Meeting, Chicago, IL.
  https://ui.adsabs.harvard.edu/abs/2022AGUFM.T25E0168B
- 1176 Cai, C., Wiens, D. A., Shen, W., & Eimer, M. (2018). Water input into the Mariana subduction 1177 zone estimated from ocean-bottom seismic data. *Nature*, *563*(7731), 389-392. 1178 doi:10.1038/s41586-018-0655-4
- 1179 Calvert, A. J., & McGeary, S. E. (2013). Seismic reflection imaging of ultradeep roots beneath 1180 the eastern Aleutian island arc. *Geology*, 41(2), 203-206. doi:10.1130/G33683.1

- 1181 Cameron, C., Prejean, S., Coombs, M., Wallace, K., Power, J., & Roman, D. (2018). Alaska
  1182 Volcano Observatory Alert and Forecasting Timeliness: 1989–2017. Frontiers in Earth
  1183 Science, 6. doi:10.3389/feart.2018.00086
- 1184 Carlson, R. L., & Miller, D. J. (2003). Mantle wedge water contents estimated from seismic velocities in partially serpentinized peridotites. *Geophysical Research Letters*, 30(5). doi:10.1029/2002GL016600
- 1187 Cerpa, N. G., Wada, I., & Wilson, C. R. (2018). Effects of fluid influx, fluid viscosity, and fluid density on fluid migration in the mantle wedge and their implications for hydrous melting. *Geosphere*, 15(1), 1-23. doi:10.1130/GES01660.1
- 1190 Christensen, D. H., & Abers, G. A. (2016). Fate and consequences of Yakutat terrane subduction
  1191 beneath eastern Alaska and the Wrangell Volcanic Field. Retrieved from:
  1192 https://www.fdsn.org/networks/detail/YG 2016/
- 1193 Christensen, D. H., & Ruff, L. J. (1988). SEISMIC COUPLING AND OUTER RISE
  1194 EARTHQUAKES. *Journal of Geophysical Research: Solid Earth*, *93*(B11), 134211195 13444. doi:https://doi.org/10.1029/JB093iB11p13421
- 1196 Christensen, N. I. (1996). Poisson's ratio and crustal seismology. *Journal of Geophysical* 1197 *Research: Solid Earth, 101*(B2), 3139-3156. doi:10.1029/95JB03446
- Clarke, J. W. (2022). Controls on bending-related faulting offshore of the Alaska Peninsula.

  Masters thesis, Northern Arizona University. Retrieved from

  https://openknowledge.nau.edu/id/eprint/5859
- 1201 Cordell, D., Naif, S., Evans, R., Key, K., Constable, S., Shillington, D., & Bécel, A. (2023).
  1202 Forearc seismogenesis in a weakly coupled subduction zone influenced by slab mantle
  1203 fluids. *Nature Geoscience*, 16(9), 822-827. doi:10.1038/s41561-023-01260-w
  - Crawford, W. C., & Webb, S. C. (2000). Identifying and Removing Tilt Noise from Low-Frequency (<0.1 Hz) Seafloor Vertical Seismic Data. *Bulletin of the Seismological Society of America*, 90(4), 952-963. doi:10.1785/0119990121
- David, C., Wong, T.-F., Zhu, W., & Zhang, J. (1994). Laboratory measurement of compactioninduced permeability change in porous rocks: Implications for the generation and maintenance of pore pressure excess in the crust. *pure and applied geophysics*, *143*(1), 425-456. doi:10.1007/BF00874337
- Davies, J., Sykes, L., House, L., & Jacob, K. (1981). Shumagin Seismic Gap, Alaska Peninsula:
  History of great earthquakes, tectonic setting, and evidence for high seismic potential.

  Journal of Geophysical Research: Solid Earth, 86(B5), 3821-3855.

  doi:https://doi.org/10.1029/JB086iB05p03821
- DeMets, C., Gordon, R. G., & Argus, D. F. (2010). Geologically current plate motions.
   *Geophysical Journal International*, 181(1), 1-80. doi:10.1111/j.1365-246X.2009.04491.x
- Drooff, C., & Freymueller, J. T. (2021). New Constraints on Slip Deficit on the Aleutian

  Megathrust and Inflation at Mt. Veniaminof, Alaska From Repeat GPS Measurements.

  Geophysical Research Letters, 48(4), e2020GL091787.

  doi:https://doi.org/10.1029/2020GL091787
- Eberhart-Phillips, D., Christensen, D. H., Brocher, T. M., Hansen, R., Ruppert, N. A., Haeussler, P. J., & Abers, G. A. (2006). Imaging the transition from Aleutian subduction to Yakutat collision in central Alaska, with local earthquakes and active source data. *Journal of Geophysical Research: Solid Earth*, 111(B11).
- doi:https://doi.org/10.1029/2005JB004240

- Eddy, C. L., & Ekström, G. (2014). Local amplification of Rayleigh waves in the continental
  United States observed on the USArray. *Earth and Planetary Science Letters*, 402, 50-57.
  doi:https://doi.org/10.1016/j.epsl.2014.01.013
- Eimer, M., Wiens, D. A., Cai, C., Lizarralde, D., & Jasperson, H. (2020). Seismicity of the Incoming Plate and Forearc Near the Mariana Trench Recorded by Ocean Bottom Seismographs. *Geochemistry, Geophysics, Geosystems, 21*(4), e2020GC008953. doi:https://doi.org/10.1029/2020GC008953
- Ekström, G. (2011). A global model of Love and Rayleigh surface wave dispersion and anisotropy, 25-250 s. *Geophysical Journal International*, 187(3), 1668-1686. doi:10.1111/j.1365-246X.2011.05225.x
- Emry, E. L., Wiens, D. A., & Garcia-Castellanos, D. (2014). Faulting within the Pacific plate at the Mariana Trench: Implications for plate interface coupling and subduction of hydrous minerals. *Journal of Geophysical Research: Solid Earth*, 119(4), 3076-3095.

  doi:https://doi.org/10.1002/2013JB010718
- Feng, L. (2021). Amphibious Shear Wave Structure Beneath the Alaska-Aleutian Subduction
  Zone From Ambient Noise Tomography. *Geochemistry, Geophysics, Geosystems, 22*(5),
  e2020GC009438. doi:https://doi.org/10.1029/2020GC009438
- Feng, L., Liu, C., & Ritzwoller, M. H. (2020). Azimuthal Anisotropy of the Crust and Uppermost Mantle Beneath Alaska. *Journal of Geophysical Research: Solid Earth*, 1245 125(12), e2020JB020076. doi:https://doi.org/10.1029/2020JB020076
- Feng, L., & Ritzwoller, M. H. (2019). A 3-D Shear Velocity Model of the Crust and Uppermost
  Mantle Beneath Alaska Including Apparent Radial Anisotropy. *Journal of Geophysical*Research: Solid Earth, 124(10), 10468-10497. doi:https://doi.org/10.1029/2019JB018122
- Fisher, M. A., & von Huene, R. E. (1982). *Map showing the geologic structure of the continental*shelf southeast and southwest of Kodiak Island, Alaska, from 24-fold seismic data (1457).
  Retrieved from <a href="http://pubs.er.usgs.gov/publication/mf1457">http://pubs.er.usgs.gov/publication/mf1457</a>
- Fujie, G., Kodaira, S., Kaiho, Y., Yamamoto, Y., Takahashi, T., Miura, S., & Yamada, T. (2018).
  Controlling factor of incoming plate hydration at the north-western Pacific margin.

  Nature Communications, 9(1), 3844. doi:10.1038/s41467-018-06320-z
- Fujie, G., Kodaira, S., Yamashita, M., Sato, T., Takahashi, T., & Takahashi, N. (2013).

  Systematic changes in the incoming plate structure at the Kuril trench. *Geophysical Research Letters*, 40(1), 88-93. doi:https://doi.org/10.1029/2012GL054340
- Furukawa, Y. (1993). Magmatic processes under arcs and formation of the volcanic front. *Journal of Geophysical Research: Solid Earth, 98*(B5), 8309-8319.

  doi:https://doi.org/10.1029/93JB00350
- Gama, I., Fischer, K. M., & Hua, J. (2022). Mapping the Lithosphere and Asthenosphere
  Beneath Alaska With Sp Converted Waves. *Geochemistry, Geophysics, Geosystems,*23(10), e2022GC010517. doi:https://doi.org/10.1029/2022GC010517
- Gou, T., Xia, S., Huang, Z., & Zhao, D. (2022). Structural Heterogeneity of the Alaska-Aleutian Forearc: Implications for Interplate Coupling and Seismogenic Behaviors. *Journal of Geophysical Research: Solid Earth*, 127(11), e2022JB024621. doi:https://doi.org/10.1029/2022JB024621
- Gou, T., Zhao, D., Huang, Z., & Wang, L. (2019). Aseismic Deep Slab and Mantle Flow
   Beneath Alaska: Insight From Anisotropic Tomography. *Journal of Geophysical Research: Solid Earth*, 124(2), 1700-1724. doi:<a href="https://doi.org/10.1029/2018JB016639">https://doi.org/10.1029/2018JB016639</a>

- Gouédard, P., Seher, T., McGuire, J. J., Collins, J. A., & van der Hilst, R. D. (2014). Correction of Ocean-Bottom Seismometer Instrumental Clock Errors Using Ambient Seismic Noise. *Bulletin of the Seismological Society of America, 104*(3), 1276-1288. doi:10.1785/0120130157
- Grevemeyer, I., Hayman, N. W., Peirce, C., Schwardt, M., Van Avendonk, H. J. A., Dannowski, A., & Papenberg, C. (2018). Episodic magmatism and serpentinized mantle exhumation at an ultraslow-spreading centre. *Nature Geoscience*, 11(6), 444-448. doi:10.1038/s41561-018-0124-6
- Hatakeyama, K., Katayama, I., Hirauchi, K.-i., & Michibayashi, K. (2017). Mantle hydration along outer-rise faults inferred from serpentinite permeability. *Scientific Reports*, 7(1), 13870. doi:10.1038/s41598-017-14309-9
- Hayes, G. P., Moore, G. L., Portner, D. E., Hearne, M., Flamme, H., Furtney, M., & Smoczyk, G. M. (2018). Slab2, a comprehensive subduction zone geometry model. *Science*, eaat4723. doi:10.1126/science.aat4723
- He, B., Wei, X., Wei, M., Shen, Y., Alvarez, M., & Schwartz, S. Y. (2023). A shallow slow slip event in 2018 in the Semidi segment of the Alaska subduction zone detected by machine learning. *Earth and Planetary Science Letters*, *612*, 118154. doi:https://doi.org/10.1016/j.epsl.2023.118154
- Hebert, L. B., Antoshechkina, P., Asimow, P., & Gurnis, M. (2009). Emergence of a low-viscosity channel in subduction zones through the coupling of mantle flow and thermodynamics. *Earth and Planetary Science Letters*, 278(3), 243-256. doi:https://doi.org/10.1016/j.epsl.2008.12.013

1294

1295

1296

1297

- Heuret, A., Conrad, C. P., Funiciello, F., Lallemand, S., & Sandri, L. (2012). Relation between subduction megathrust earthquakes, trench sediment thickness and upper plate strain. *Geophysical Research Letters*, *39*(5). doi:https://doi.org/10.1029/2011GL050712
- Horowitz, W. L., Steffy, D. A., Hoose, P. J., & Turner, R. F. (1989). *Geologic report for the Shumagin planning area, western Gulf of Alaska. Final report*. Retrieved from United States: https://www.osti.gov/biblio/6911563
- Hyndman, R. D., & Peacock, S. M. (2003). Serpentinization of the forearc mantle. *Earth and Planetary Science Letters*, 212(3), 417-432. doi:<a href="https://doi.org/10.1016/S0012-821X(03)00263-2">https://doi.org/10.1016/S0012-821X(03)00263-2</a>
- 1302 IRIS Transportable Array. (2003). *USArray Transportable Array*. Retrieved from: https://www.fdsn.org/networks/detail/TA/
- Ivandic, M., Grevemeyer, I., Berhorst, A., Flueh, E. R., & McIntosh, K. (2008). Impact of
   bending related faulting on the seismic properties of the incoming oceanic plate offshore
   of Nicaragua. *Journal of Geophysical Research: Solid Earth*, 113(B5).
   doi:<a href="https://doi.org/10.1029/2007JB005291">https://doi.org/10.1029/2007JB005291</a>
- Janiszewski, H. A., Abers, G. A., Shillington, D. J., & Calkins, J. A. (2013). Crustal structure along the Aleutian island arc: New insights from receiver functions constrained by active-source data. *Geochemistry, Geophysics, Geosystems, 14*(8), 2977-2992. doi:<a href="https://doi.org/10.1002/ggge.20211">https://doi.org/10.1002/ggge.20211</a>
- Janiszewski, H. A., Gaherty, J. B., Abers, G. A., Gao, H., & Eilon, Z. C. (2019). Amphibious surface-wave phase-velocity measurements of the Cascadia subduction zone. *Geophysical Journal International*, 217(3), 1929-1948. doi:10.1093/gji/ggz051
- Ji, S., Li, A., Wang, Q., Long, C., Wang, H., Marcotte, D., & Salisbury, M. (2013). Seismic velocities, anisotropy, and shear-wave splitting of antigorite serpentinites and tectonic

- implications for subduction zones. *Journal of Geophysical Research: Solid Earth, 118*(3), 1015-1037. doi:https://doi.org/10.1002/jgrb.50110
- Jiang, C., Schmandt, B., Ward, K. M., Lin, F.-C., & Worthington, L. L. (2018). Upper Mantle
   Seismic Structure of Alaska From Rayleigh and S Wave Tomography. *Geophysical Research Letters*, 45(19), 10,350-310,359. doi:<a href="https://doi.org/10.1029/2018GL079406">https://doi.org/10.1029/2018GL079406</a>
- Jiang, Y., González, P. J., & Bürgmann, R. (2022). Subduction earthquakes controlled by
   incoming plate geometry: The 2020 M > 7.5 Shumagin, Alaska, earthquake doublet.
   *Earth and Planetary Science Letters*, 584, 117447.
   doi:https://doi.org/10.1016/j.epsl.2022.117447
- Jin, G., & Gaherty, J. B. (2015). Surface wave phase-velocity tomography based on multichannel cross-correlation. *Geophysical Journal International*, 201(3), 1383-1398. doi:10.1093/gji/ggv079
- Kahrizi, A., Delescluse, M., Chamot-Rooke, N., Pubellier, M., Bécel, A., Shillington, D., . . . Bulois, C. (2024). Extensional forearc structures at the transition from Alaska to Aleutian Subduction Zone: slip partitioning, terranes and large earthquakes. *Comptes Rendus*. *Géoscience*. doi:10.5802/crgeos.225
- Korenaga, J. (2017). On the extent of mantle hydration caused by plate bending. *Earth and Planetary Science Letters*, 457, 1-9. doi:https://doi.org/10.1016/j.epsl.2016.10.011
- Korenaga, J., Planavsky, N. J., & Evans, D. A. D. (2017). Global water cycle and the coevolution of the Earth's interior and surface environment. *Philosophical Transactions of the Royal Society A: Mathematical, Physical and Engineering Sciences, 375*(2094), 20150393. doi:10.1098/rsta.2015.0393
- Kuehn, H. (2019). Along-trench segmentation and down-dip limit of the seismogenic zone at the eastern Alaska-Aleutian subduction zone.
- Kustowski, B., Ekström, G., & Dziewoński, A. M. (2008). Anisotropic shear-wave velocity structure of the Earth's mantle: A global model. *Journal of Geophysical Research: Solid Earth*, 113(B6). doi:https://doi.org/10.1029/2007JB005169
- Li, J., Shillington, D. J., Bécel, A., Nedimović, M. R., Webb, S. C., Saffer, D. M., . . . Kuehn, H. (2015). Downdip variations in seismic reflection character: Implications for fault structure and seismogenic behavior in the Alaska subduction zone. *Journal of Geophysical Research: Solid Earth*, 120(11), 7883-7904. doi:https://doi.org/10.1002/2015JB012338
- Li, J., Shillington, D. J., Saffer, D. M., Bécel, A., Nedimović, M. R., Kuehn, H., . . . Abers, G. A. (2018). Connections between subducted sediment, pore-fluid pressure, and earthquake behavior along the Alaska megathrust. *Geology*, 46(4), 299-302. doi:10.1130/G39557.1
- Li, S., & Freymueller, J. T. (2018). Spatial Variation of Slip Behavior Beneath the Alaska
  Peninsula Along Alaska-Aleutian Subduction Zone. *Geophysical Research Letters*, 45(8),
  3453-3460. doi:https://doi.org/10.1002/2017GL076761
- Ligorría, J. P., & Ammon, C. J. (1999). Iterative deconvolution and receiver-function estimation.

  Bulletin of the Seismological Society of America, 89(5), 1395-1400.
- Lin, F.-C., Moschetti, M. P., & Ritzwoller, M. H. (2008). Surface wave tomography of the western United States from ambient seismic noise: Rayleigh and Love wave phase velocity maps. *Geophysical Journal International*, 173(1), 281-298. doi:10.1111/j.1365-246X.2008.03720.x

- Lin, F.-C., & Ritzwoller, M. H. (2011). Helmholtz surface wave tomography for isotropic and azimuthally anisotropic structure. *Geophysical Journal International*, 186(3), 1104-1120. doi:10.1111/j.1365-246X.2011.05070.x
- Lin, F.-C., Ritzwoller, M. H., & Snieder, R. (2009). Eikonal tomography: surface wave tomography by phase front tracking across a regional broad-band seismic array. *Geophysical Journal International*, 177(3), 1091-1110. doi:10.1111/j.1365-246X.2009.04105.x
- Lin, F.-C., Tsai, V. C., & Ritzwoller, M. H. (2012). The local amplification of surface waves: A new observable to constrain elastic velocities, density, and anelastic attenuation. *Journal of Geophysical Research: Solid Earth, 117*(B6).

  doi:https://doi.org/10.1029/2012JB009208
- Liu, C., Bai, Y., Lay, T., Feng, Y., & Xiong, X. (2023). Megathrust complexity and the up-dip extent of slip during the 2021 Chignik, Alaska Peninsula earthquake. *Tectonophysics*, 854, 229808. doi:https://doi.org/10.1016/j.tecto.2023.229808
- Liu, C., Lay, T., & Xiong, X. (2022). The 29 July 2021 MW 8.2 Chignik, Alaska Peninsula Earthquake Rupture Inferred From Seismic and Geodetic Observations: Re-Rupture of the Western 2/3 of the 1938 Rupture Zone. *Geophysical Research Letters*, 49(4), e2021GL096004. doi:https://doi.org/10.1029/2021GL096004
- Liu, C., Lay, T., Xiong, X., & Wen, Y. (2020). Rupture of the 2020 MW 7.8 Earthquake in the
  Shumagin Gap Inferred From Seismic and Geodetic Observations. *Geophysical Research*Letters, 47(22), e2020GL090806. doi:https://doi.org/10.1029/2020GL090806
- Liu, C., Zhang, S., Sheehan, A. F., & Ritzwoller, M. H. (2022). Surface Wave Isotropic and Azimuthally Anisotropic Dispersion Across Alaska and the Alaska-Aleutian Subduction Zone. *Journal of Geophysical Research: Solid Earth, 127*(11), e2022JB024885. doi:https://doi.org/10.1029/2022JB024885
- Lonsdale, P. (1988). Paleogene history of the Kula plate: Offshore evidence and onshore implications. *GSA Bulletin*, 100(5), 733-754. doi:10.1130/0016-7606(1988)100<0733:PHOTKP>2.3.CO;2
- Lynner, C. (2021). Anisotropy-revealed change in hydration along the Alaska subduction zone. *Geology*. doi:10.1130/G48860.1
- Ma, Z., Dalton, C. A., Russell, J. B., Gaherty, J. B., Hirth, G., & Forsyth, D. W. (2020). Shear attenuation and anelastic mechanisms in the central Pacific upper mantle. *Earth and Planetary Science Letters*, *536*, 116148. doi:https://doi.org/10.1016/j.epsl.2020.116148
- Manea, V. C., Leeman, W. P., Gerya, T., Manea, M., & Zhu, G. (2014). Subduction of fracture zones controls mantle melting and geochemical signature above slabs. *Nature Communications*, *5*(1), 5095. doi:10.1038/ncomms6095
- Mark, H. F., Lizarralde, D., & Wiens, D. A. (2023). Constraints on Bend-Faulting and Mantle Hydration at the Marianas Trench From Seismic Anisotropy. *Geophysical Research* Letters, 50(10), e2023GL103331. doi:https://doi.org/10.1029/2023GL103331
- Marlow, M. S., Cooper, A. K., & Fisher, M. A. (1994). Geology of the eastern Bering Sea continental shelf. In G. Plafker & H. C. Berg (Eds.), *The Geology of Alaska* (Vol. G-1, pp. 0). doi:10.1130/DNAG-GNA-G1.271
- Martin-Short, R., Allen, R., Bastow, I. D., Porritt, R. W., & Miller, M. S. (2018). Seismic
  Imaging of the Alaska Subduction Zone: Implications for Slab Geometry and Volcanism. *Geochemistry, Geophysics, Geosystems, 19*(11), 4541-4560. doi:10.1029/2018GC007962

- 1406 Masson, D. G. (1991). Fault patterns at outer trench walls. *Marine Geophysical Researches*, 1407 *13*(3), 209-225. doi:10.1007/BF00369150
- Matulka, P., & Wiens, D. (2022). Heterogeneous Plate-Bending Earthquake Distribution and
   Focal Mechanisms Along the Alaska Subduction Zone. Paper presented at the AGU Fall
   Meeting, Chicago, IL. <a href="https://ui.adsabs.harvard.edu/abs/2022AGUFM.T32C..03M">https://ui.adsabs.harvard.edu/abs/2022AGUFM.T32C..03M</a>
- McKenzie, D., Jackson, J., & Priestley, K. (2005). Thermal structure of oceanic and continental lithosphere. *Earth and Planetary Science Letters*, 233(3), 337-349. doi:https://doi.org/10.1016/j.epsl.2005.02.005
- Meyer, B., Chulliat, A., & Saltus, R. (2017). Derivation and Error Analysis of the Earth Magnetic Anomaly Grid at 2 arc min Resolution Version 3 (EMAG2v3). *Geochemistry*, *Geophysics, Geosystems*, 18(12), 4522-4537. doi:https://doi.org/10.1002/2017GC007280
- Miller, N. C., & Lizarralde, D. (2016). Finite-frequency wave propagation through outer rise fault zones and seismic measurements of upper mantle hydration. *Geophysical Research Letters*, 43(15), 7982-7990. doi:10.1002/2016GL070083
- Miller, N. C., Lizarralde, D., Collins, J. A., Holbrook, W. S., & Van Avendonk, H. J. A. (2021).
   Limited Mantle Hydration by Bending Faults at the Middle America Trench. *Journal of Geophysical Research: Solid Earth*, *126*(1), e2020JB020982.
   doi:<a href="https://doi.org/10.1029/2020JB020982">https://doi.org/10.1029/2020JB020982</a>
- Moore, J. C., Diebold, J., Fisher, M. A., Sample, J., Brocher, T., Talwani, M., . . . Sawyer, D. (1991). EDGE deep seismic reflection transect of the eastern Aleutian arc-trench layered lower crust reveals underplating and continental growth. *Geology*, 19(5), 420-424. doi:10.1130/0091-7613(1991)019<0420:EDSRTO>2.3.CO;2
- Moschetti, M. P., Ritzwoller, M. H., Lin, F. C., & Yang, Y. (2010). Crustal shear wave velocity structure of the western United States inferred from ambient seismic noise and earthquake data. *Journal of Geophysical Research: Solid Earth*, *115*(B10). doi:https://doi.org/10.1029/2010JB007448
- Nakatani, T., & Nakamura, M. (2016). Experimental constraints on the serpentinization rate of fore-arc peridotites: Implications for the upwelling condition of the slab-derived fluid. *Geochemistry, Geophysics, Geosystems, 17*(8), 3393-3419.

  doi:https://doi.org/10.1002/2016GC006295
- Naliboff, J. B., Billen, M. I., Gerya, T., & Saunders, J. (2013). Dynamics of outer-rise faulting in oceanic-continental subduction systems. *Geochemistry, Geophysics, Geosystems, 14*(7), 2310-2327. doi:https://doi.org/10.1002/ggge.20155
- Nishikawa, T., & Ide, S. (2015). Background seismicity rate at subduction zones linked to slabbending-related hydration. *Geophysical Research Letters*, 42(17), 7081-7089. doi:https://doi.org/10.1002/2015GL064578
- NOAA, National Oceanic Atmospheric Administration. (1967). National Tsunami Warning
   Center Alaska Seismic Network. Retrieved from:
   <a href="https://www.fdsn.org/networks/detail/AT/">https://www.fdsn.org/networks/detail/AT/</a>
- Okamoto, A., Ogasawara, Y., Ogawa, Y., & Tsuchiya, N. (2011). Progress of hydration reactions in olivine–H2O and orthopyroxenite–H2O systems at 250°C and vapor-saturated pressure. *Chemical Geology*, 289(3), 245-255. doi:https://doi.org/10.1016/j.chemgeo.2011.08.007
- Qi, C., Zhao, D., Chen, Y., & Ruppert, N. A. (2007). New insight into the crust and upper mantle structure under Alaska. *Polar Science*, 1(2), 85-100. doi:https://doi.org/10.1016/j.polar.2007.07.001

- Ranero, C. R., Phipps Morgan, J., McIntosh, K., & Reichert, C. (2003). Bending-related faulting and mantle serpentinization at the Middle America trench. *Nature*, 425(6956), 367-373. doi:10.1038/nature01961
- Rees Jones, D. W., Katz, R. F., Tian, M., & Rudge, J. F. (2018). Thermal impact of magmatism in subduction zones. *Earth and Planetary Science Letters*, 481, 73-79. doi:https://doi.org/10.1016/j.epsl.2017.10.015
- Reynard, B. (2013). Serpentine in active subduction zones. *Lithos*, *178*, 171-185. doi:https://doi.org/10.1016/j.lithos.2012.10.012
- Richards, F. D., Hoggard, M. J., Cowton, L. R., & White, N. J. (2018). Reassessing the Thermal Structure of Oceanic Lithosphere With Revised Global Inventories of Basement Depths and Heat Flow Measurements. *Journal of Geophysical Research: Solid Earth, 123*(10), 9136-9161. doi:https://doi.org/10.1029/2018JB015998
- Ruff, L. J. (1989). Do trench sediments affect great earthquake occurrence in subduction zones? pure and applied geophysics, 129(1), 263-282. doi:10.1007/BF00874629
- Ruppert, N. A., Barcheck, G., & Abers, G. A. (2022). Enhanced Regional Earthquake Catalog with Alaska Amphibious Community Seismic Experiment Data. *Seismological Research Letters*, 94(1), 522-530. doi:10.1785/0220220226
- Russell, J. B., & Dalton, C. A. (2022). Rayleigh Wave Attenuation and Amplification Measured at Ocean-Bottom Seismometer Arrays Using Helmholtz Tomography. *Journal of Geophysical Research: Solid Earth*, *127*(10), e2022JB025174. doi:https://doi.org/10.1029/2022JB025174
- Sadofsky, S. J., Portnyagin, M., Hoernle, K., & van den Bogaard, P. (2008). Subduction cycling of volatiles and trace elements through the Central American volcanic arc: evidence from melt inclusions. *Contributions to Mineralogy and Petrology*, 155(4), 433-456. doi:10.1007/s00410-007-0251-3
- Sallarès, V., & Ranero, C. R. (2019). Upper-plate rigidity determines depth-varying rupture behaviour of megathrust earthquakes. *Nature*, *576*(7785), 96-101. doi:10.1038/s41586-019-1784-0
- Sample, J. C., & Moore, J. C. (1987). Structural style and kinematics of an underplated slate belt, Kodiak and adjacent islands, Alaska. *GSA Bulletin*, 99(1), 7-20. doi:10.1130/0016-7606(1987)99<7:SSAKOA>2.0.CO;2
- Sandiford, D., & Craig, T. J. (2023). Plate bending earthquakes and the strength distribution of the lithosphere. *Geophysical Journal International*, 235(1), 488-508. doi:10.1093/gji/ggad230
- Scholl, D. W., Kirby, S. H., von Huene, R., Ryan, H., Wells, R. E., & Geist, E. L. (2015). Great (≥Mw8.0) megathrust earthquakes and the subduction of excess sediment and bathymetrically smooth seafloor. *Geosphere*, 11(2), 236-265. doi:10.1130/GES01079.1
- Schwartz, S., Guillot, S., Reynard, B., Lafay, R., Debret, B., Nicollet, C., . . . Auzende, A. L. (2013). Pressure–temperature estimates of the lizardite/antigorite transition in high pressure serpentinites. *Lithos*, 178, 197-210. doi:<a href="https://doi.org/10.1016/j.lithos.2012.11.023">https://doi.org/10.1016/j.lithos.2012.11.023</a>
- Scripps Institution of Oceanography. (1986). *Global Seismograph Network IRIS/IDA*.

  Retrieved from: https://www.fdsn.org/networks/detail/II/
- Shellenbaum, D. P., Gregersen, L. S., & Delaney, P. R. (2010). Top Mesozoic unconformity depth map of the Cook Inlet Basin, Alaska, Alaska Div. *Geol. Geophys. Surv. Report of Investigation*, 2(1).

- Shen, W., & Ritzwoller, M. H. (2016). Crustal and uppermost mantle structure beneath the
  United States. *Journal of Geophysical Research: Solid Earth*, 121(6), 4306-4342.
  doi:https://doi.org/10.1002/2016JB012887
- Shen, W., Ritzwoller, M. H., Kang, D., Kim, Y., Lin, F.-C., Ning, J., . . . Zhou, L. (2016). A seismic reference model for the crust and uppermost mantle beneath China from surface wave dispersion. *Geophysical Journal International*, 206(2), 954-979. doi:10.1093/gji/ggw175
- Shen, W., Ritzwoller, M. H., Schulte-Pelkum, V., & Lin, F.-C. (2013). Joint inversion of surface wave dispersion and receiver functions: a Bayesian Monte-Carlo approach. *Geophysical Journal International*, 192(2), 807-836. doi:10.1093/gji/ggs050
- Shen, W., Wiens, D. A., Anandakrishnan, S., Aster, R. C., Gerstoft, P., Bromirski, P. D., . . .

  Winberry, J. P. (2018). The Crust and Upper Mantle Structure of Central and West

  Antarctica From Bayesian Inversion of Rayleigh Wave and Receiver Functions. *Journal*of Geophysical Research: Solid Earth, 123(9), 7824-7849.

  doi:https://doi.org/10.1029/2017JB015346
- Shillington, D. J., Bécel, A., & Nedimović, M. R. (2022). Upper Plate Structure and Megathrust
  Properties in the Shumagin Gap Near the July 2020 M7.8 Simeonof Event. *Geophysical*Research Letters, 49(2), e2021GL096974. doi:https://doi.org/10.1029/2021GL096974
- Shillington, D. J., Bécel, A., Nedimović, M. R., Kuehn, H., Webb, S. C., Abers, G. A., . . . Mattei-Salicrup, G. A. (2015). Link between plate fabric, hydration and subduction zone seismicity in Alaska. *Nature Geoscience*, 8(12), 961-964. doi:10.1038/ngeo2586
- Silwal, V., Tape, C., & Lomax, A. (2018). Crustal earthquakes in the Cook Inlet and Susitna region of southern Alaska. *Tectonophysics*, 745, 245-263. doi:https://doi.org/10.1016/j.tecto.2018.08.013
- Stehly, L., Campillo, M., & Shapiro, N. M. (2007). Traveltime measurements from noise correlation: stability and detection of instrumental time-shifts. *Geophysical Journal International*, 171(1), 223-230. doi:10.1111/j.1365-246X.2007.03492.x
- Stein, C. A., & Stein, S. (1992). A model for the global variation in oceanic depth and heat flow with lithospheric age. *Nature*, *359*(6391), 123-129. doi:10.1038/359123a0
- Takei, Y. (2002). Effect of pore geometry on VP/VS: From equilibrium geometry to crack. *Journal of Geophysical Research: Solid Earth, 107*(B2), ECV 6-1-ECV 6-12.

  doi:https://doi.org/10.1029/2001JB000522
- Thybo, H., & Artemieva, I. M. (2013). Moho and magmatic underplating in continental lithosphere. *Tectonophysics*, 609, 605-619. doi:https://doi.org/10.1016/j.tecto.2013.05.032
- Tian, Y., & Ritzwoller, M. H. (2017). Improving ambient noise cross-correlations in the noisy ocean bottom environment of the Juan de Fuca plate. *Geophysical Journal International*, 210(3), 1787-1805. doi:10.1093/gji/ggx281
- Tian, Y., & Zhao, D. (2012). Seismic anisotropy and heterogeneity in the Alaska subduction zone. *Geophysical Journal International*, 190(1), 629-649. doi:10.1111/j.1365-246X.2012.05512.x
- U. S. Geological Survey. (2016). *U.S. Geological Survey Networks*. Retrieved from: https://www.fdsn.org/networks/detail/GM/
- Van Avendonk, H. J. A., Holbrook, W. S., Lizarralde, D., & Denyer, P. (2011). Structure and serpentinization of the subducting Cocos plate offshore Nicaragua and Costa Rica. *Geochemistry, Geophysics, Geosystems, 12*(6). doi:10.1029/2011GC003592

- van Keken, P. E., Hacker, B. R., Syracuse, E. M., & Abers, G. A. (2011). Subduction factory: 4.

  Depth-dependent flux of H2O from subducting slabs worldwide. *Journal of Geophysical Research: Solid Earth*, *116*(B1). doi:https://doi.org/10.1029/2010JB007922
- von Huene, R., Miller, J. J., & Krabbenhoeft, A. (2019). The Shumagin seismic gap structure and associated tsunami hazards, Alaska convergent margin. *Geosphere*, 15(2), 324-341. doi:10.1130/GES01657.1
- von Huene, R., Miller, J. J., & Krabbenhoeft, A. (2021). The Alaska Convergent Margin
  Backstop Splay Fault Zone, a Potential Large Tsunami Generator Between the Frontal
  Prism and Continental Framework. *Geochemistry, Geophysics, Geosystems, 22*(1),
  e2019GC008901. doi:https://doi.org/10.1029/2019GC008901
- von Huene, R., Miller, J. J., & Weinrebe, W. (2012). Subducting plate geology in three great earthquake ruptures of the western Alaska margin, Kodiak to Unimak. *Geosphere*, 8(3), 628-644. doi:10.1130/GES00715.1
- Walker, K. T., McGeary, S. E., & Klemperer, S. L. (2003). Tectonic Evolution of the Bristol Bay basin, southeast Bering Sea: Constraints from seismic reflection and potential field data. *Tectonics*, 22(5). doi:https://doi.org/10.1029/2002TC001359
- Wang, F., Wei, S. S., Elliott, J., Freymueller, J. T., Drooff, C., Ruppert, N. A., & Zhang, H.
   (2022). Subduction fluids control slab slip behaviors and megathrust earthquakes at the
   Alaska Peninsula. <a href="https://ui.adsabs.harvard.edu/abs/2022AGUFM.T32C..07W">https://ui.adsabs.harvard.edu/abs/2022AGUFM.T32C..07W</a>
- Wang, Y., & Tape, C. (2014). Seismic velocity structure and anisotropy of the Alaska subduction zone based on surface wave tomography. *Journal of Geophysical Research: Solid Earth*, 119(12), 8845-8865. doi:https://doi.org/10.1002/2014JB011438
- Ward, K. M. (2015). Ambient noise tomography across the southern Alaskan Cordillera. *Geophysical Research Letters*, 42(9), 3218-3227.

  doi:https://doi.org/10.1002/2015GL063613

1570

- Ward, K. M., & Lin, F.-C. (2018). Lithospheric Structure Across the Alaskan Cordillera From the Joint Inversion of Surface Waves and Receiver Functions. *Journal of Geophysical Research: Solid Earth*, 123(10), 8780-8797. doi:https://doi.org/10.1029/2018JB015967
- Webb, S. C., & Crawford, W. C. (1999). Long-period seafloor seismology and deformation under ocean waves. *Bulletin of the Seismological Society of America*, 89(6), 1535-1542.
- Wei, S. S., Ruprecht, P., Gable, S. L., Huggins, E. G., Ruppert, N., Gao, L., & Zhang, H. (2021).

  Along-strike variations in intermediate-depth seismicity and arc magmatism along the
  Alaska Peninsula. *Earth and Planetary Science Letters*, *563*, 116878.

  doi:https://doi.org/10.1016/j.epsl.2021.116878
- Wessel, P., Luis, J. F., Uieda, L., Scharroo, R., Wobbe, F., Smith, W. H. F., & Tian, D. (2019).

  The Generic Mapping Tools Version 6. *Geochemistry, Geophysics, Geosystems, 20*(11),

  5556-5564. doi:<a href="https://doi.org/10.1029/2019GC008515">https://doi.org/10.1029/2019GC008515</a>
- Wiens, D. A., Conder, J. A., & Faul, U. H. (2008). The Seismic Structure and Dynamics of the Mantle Wedge. *Annual Review of Earth and Planetary Sciences*, *36*(1), 421-455. doi:10.1146/annurev.earth.33.092203.122633
- Wilson, C. R., Spiegelman, M., van Keken, P. E., & Hacker, B. R. (2014). Fluid flow in
   subduction zones: The role of solid rheology and compaction pressure. *Earth and Planetary Science Letters*, 401, 261-274. doi:<a href="https://doi.org/10.1016/j.epsl.2014.05.052">https://doi.org/10.1016/j.epsl.2014.05.052</a>
- Wilson, F. H., Hults, C., Mull, C. G., & Karl, S. M. (2015). *Geologic map of Alaska* (3340).

  Retrieved from Reston, VA: <a href="https://pubs.usgs.gov/publication/sim3340">https://pubs.usgs.gov/publication/sim3340</a>

- Xiao, Z., Freymueller, J. T., Grapenthin, R., Elliott, J. L., Drooff, C., & Fusso, L. (2021). The
   deep Shumagin gap filled: Kinematic rupture model and slip budget analysis of the 2020
   Mw 7.8 Simeonof earthquake constrained by GNSS, global seismic waveforms, and
   floating InSAR. *Earth and Planetary Science Letters*, 576, 117241.
   doi:https://doi.org/10.1016/j.epsl.2021.117241
- Yang, X., & Gao, H. (2020). Segmentation of the Aleutian-Alaska Subduction Zone Revealed by Full-Wave Ambient Noise Tomography: Implications for the Along-Strike Variation of Volcanism. *Journal of Geophysical Research: Solid Earth*, *125*(11), e2020JB019677. doi:https://doi.org/10.1029/2020JB019677
- Ye, S., Flueh, E. R., Klaeschen, D., & von Huene, R. (1997). Crustal structure along the EDGE transect beneath the Kodiak shelf off Alaska derived from OBH seismic refraction data. *Geophysical Journal International*, 130(2), 283-302. doi:10.1111/j.1365-246X.1997.tb05648.x
- Zhao, D., Wang, Z., Umino, N., & Hasegawa, A. (2007). Tomographic Imaging outside a
   Seismic Network: Application to the Northeast Japan Arc. *Bulletin of the Seismological* Society of America, 97(4), 1121-1132. doi:10.1785/0120050256
- Zhu, G., Wiens, D. A., Yang, H., Lin, J., Xu, M., & You, Q. (2021). Upper Mantle Hydration
   Indicated by Decreased Shear Velocity Near the Southern Mariana Trench From
   Rayleigh Wave Tomography. *Geophysical Research Letters*, 48(15), e2021GL093309.
   doi: <a href="https://doi.org/10.1029/2021GL093309">https://doi.org/10.1029/2021GL093309</a>